General information of the article

Type of paper: Article

Title: A state-dependent constitutive model for coarse-grained gassy soil and its application in slope instability modelling

Authors: Yi Hong, Xuetao Wang, Lizhong Wang*, Zhiwei Gao

*Corresponding author

Information of the authors

Corresponding author: Dr Lizhong Wang

Qiushi Distinguished Professor, Key Laboratory of Offshore Geotechnics and Material of Zhejiang Province, College of Civil Engineering and Architecture, Zhejiang University, China

Email: wanglz@zju.edu.cn

Co-author: Dr Yi Hong

Associate Professor, Key Laboratory of Offshore Geotechnics and Material of Zhejiang Province, College of Civil Engineering and Architecture, Zhejiang University, China

Email: yi_hong@zju.edu.cn

Tel.: 13758906685

Co-author: Mr Xuetao Wang

Research student, Key Laboratory of Offshore Geotechnics and Material of Zhejiang Province, College of Civil Engineering and Architecture, Zhejiang University, China

Email: xuetao_wang@zju.edu.cn

Co-author: Dr Zhiwei Gao

Lecturer, James Watt School of Engineering, University of Glasgow, Glasgow, G12 8QQ, UK.

Email: Zhiwei.gao@glasgow.ac.uk

A state-dependent constitutive model for coarse-grained gassy soil and its application in slope instability modelling

Abstract

Free gas in sandy marine sediments is a common occurrence worldwide. A distinct feature of gassy sand is that, under undrained shearing, presence of occluded gas bubbles in the pore fluid can increase the undrained strength of sand at a relatively loose state, while reduce the strength of a relatively dense sand. Previous theoretical analyses have primarily focused on modelling the 'beneficial' effect of free gas on loose sand in migrating static liquefaction, with few attempts to describe the 'detrimental' effect of gas on dense sand under undrained loading. This study presents a state-dependent critical state model, which describes the distinct behavior of gassy sand with various states in a unified way. Comparison between the model predictions and test data of three gassy sands shows that the new model can capture the constitutive behavior of gassy marine sand over a wide range of initial states and degrees of saturation (typically between 85% and 100% for unsaturated marine sediments) using a single set of parameters. Parametric studies were performed to quantify the effects of gas (either 'detrimental' or 'beneficial') on sand with various initial states. The new model has been implemented in ABAQUS and used to simulate the stability of submarine slopes under undrained loading condition. It is found that free gas can improve and weaken the slope stability for loose and dense sand, respectively.

***Key words*:** gassy sand, constitutive modelling, finite element analysis, static liquefaction, slope stability

1. Introduction

Free gas is widely formed in the marine sediments throughout the world, including the North Sea, Gulf of Mexico, Gulf of Guinea, Gulf Coast and Eastern China Sea (Sobkowicz & Morgenstern, 1984; Rad & Lunne, 1994; Hight and Leroueil 2003; Sultan & Garziglia, 2014; Rowe & Mabrouk, 2018; Jommi et al., 2019). The gas in marine sediments is typically methane, produced by decomposition of organic matter (Wheeler, 1988) or gas hydrates (Grozic et al., 1999; Sánchez et al., 2017). It is certain that global warming will cause more methane generation in both offshore and onshore soils, as the decompositions are faster at higher temperature (Milich, 1999; Stagg et al., 2017). In addition to the naturally formed gas in sediments, gas has also been introduced artificially into the soil through biological mediation or blasting, aiming to increase the strength (Rebata-Landa & Santamarina 2012; Finno & Gallant, 2016) or facilitate consolidation of the gas-charged soil (Puzrin et al. 2011). These gassy soils are largely different from the conventional unsaturated soils, in view of their high degree of saturation (S_r≥80%) along with the discontinuous gas phase in bubble form (Hong et al., 2019a).

A unique feature of the gassy soil, as revealed experimentally, is that the gas bubbles can either weaken or strengthen the shear strength of both fine-grained and coarse-gained soil, depending on the initial states (Wheeler, 1986; Grozic et al., 1999; He & Chu, 2014; Vega-Posada et al., 2014; Hong et al., 2019b; Yang et al., 2019). Increasing offshore construction activities on gas-bearing seabed have generated interests in developing theoretical models of gassy soils. For fine-grained gassy soil, constitutive models that enable a unified description of both 'detrimental' and 'beneficial' effects of gas on the host soil have been developed, by formulating gas-dependent yielding function, dilation function and hardening law (Gao et al., 2020; Hong et al., 2020). While for coarse-grained gassy soil, previous theoretical developments have primarily focused on modelling the 'beneficial' effect of gas on loose sand in migrating static liquefaction (Pietruszczak & Pande, 1996; Grozic et al., 2005; Lü et al., 2018), with few attempts to describe the 'detrimental' effect of gas on dense sand under undrained loading.

Fig. 1(a) shows a schematic diagram of the internal structure of coarse-grained gassy soils, where discrete gas bubbles are typically smaller than the soil particles and present in the pore water. Coarse-grained gassy soil can thus be considered as a saturated soil with compressible pore fluid. Based on this consideration, Pietruszczak & Pande (1996) and Lü et al. (2018) have developed elasto-plastic models for gassy sand and validated their models against results of loose gassy sand. Since these studies have not focused on modelling of dense gassy sand, they employed simplified functional forms of plastic modulus (K_{p}), which do not consider softening behavior of dense sands (i.e., the K_{p} cannot be negative). Grozic et al. (2005) have also presented a gassy sand model, which is shown to satisfactorily predict results of for loose gassy sand but cannot properly capture the response of unsaturated dense sand. It is thus desirable to develop a constitutive model for gassy sand that can describe their response at various initial states in a unified manner.

Free gas in sand deposits also affects the offshore foundation design, drilling procedures, slope stability, and may even have an environmental impact (Grozic et al., 2005). Existing research has primarily focused on the element response of gassy sand in triaxial tests, with little work on the real engineering problems. Atigh & Byrne (2004) have shown that free gas can enhance the stability of loose sand slopes under undrained condition. But the sand density can vary significantly in the field and dense sand slopes are more common. Therefore, more comprehensive research on gassy sand problems in the field is needed.

A state-dependent model for coarse-grained gassy soil is formulated in this study. The predictive capability of the model was validated against three gassy sands with different initial states (including dense and loose states) and degrees of saturation and compared to that of the existing gassy sand models. Parametric studies were performed to quantify the effect of gas on gassy sand with various initial states. The new model has also been implemented in a finite element code and used to analyze the stability of submarine slopes under undrained condition. The effect of sand density has been investigated.

2. A state-dependent constitutive model for coarse-grained gassy soil

To facilitate the discussion, the model described in this section is presented in the triaxial stress space. Generalized expressions of the model under the multi-axial loading conditions are described in the Appendix. In the triaxial stress space, two stress qua``ntities including the mean total stress $p = (\sigma_a + 2\sigma_r)/3$ and deviator stress $q = \sigma_a - \sigma_r$ are used, where σ_a is the total axial stress and σ_r is the total radial stress. The stress quantities with the symbol $'$ are effective ones.

2.1 Compressibility of gas-fluid mixture: role of gas compression and dissolution

For gassy sand, the gas bubbles are much smaller than the sand particles, and thus mainly affect the compressibility of the pore water. The compressibility of the gas-water mixture depends on the amounts of free and dissolved gases, which change with excess pore water pressure. This sub-section presents the derivation of compressibility of the gas-water mixture (Fredlund & Rahardjo, 1993), based on the three-phase diagram considering gas compression and dissolution, as illustrated in Fig. 1(b).

It is shown in Fredlund & Rahardjo (1993) that the compressibility of a gas-water mixture C_{aw} is expressed as:

$$C_{\mathrm{aw}}=-\frac{d(V_{\mathrm{a}}+V_{\mathrm{w}})}{(V_{\mathrm{a}}+V_{\mathrm{w}})dp}=-\frac{1}{V_{\mathrm{a}}+V_{\mathrm{w}}}\left\{\frac{\mathrm{d}(V_{\mathrm{w}}-V_{\mathrm{d}})}{\mathrm{d}p}+\frac{\mathrm{d}(V_{\mathrm{a}}+V_{\mathrm{d}})}{\mathrm{d}p}\right\} \tag{1}$$

where V_{w} is the volume of pore water. V_{a} and V_{d} are the volumes of free gas in pore water and gas dissolved in pore water, respectively. p is the mean total stress. The difference between the pore water pressure u_{w} and pore air pressure u_{a} is only related to the radius R of the gas bubble and the surface tension T, i.e., u_{a}-u_{w}=2T/R, if the minor effect of vapour pressure in each bubble (Wheeler et al., 1988a) were ignored. The value of T for a water-air interface is approximately 0.073 N/m (Weast, 1984). On the other hand, the mean value of R for bubbles in gassy sand normally between 0.17 and 0.25 mm, as measured by micro-computed tomography (μCT) on gassy specimens under in-situ stresses (Zhang, 2020). It can be readily deduced that the mean value of u_{a}-u_{w} for gassy sand may range between 0.6 and 0.9 kPa. In other words, u_{w} and u_{a} in gassy sand are likely to be very close in value, as routinely assumed for gassy sand (Sobkowicz & Morgenstern, 1984; Pietruszczak & Pande, 1996; Grozic et al., 2005).

One can get the following using the chain rule of differentiation to Eq. (1):

$$C_{\mathrm{aw}}=-\frac{1}{V_{\mathrm{a}}+V_{\mathrm{w}}}\left\{\frac{\mathrm{d}V_{\mathrm{w}}}{du_{\mathrm{w}}}\frac{du_{\mathrm{w}}}{\mathrm{d}p}+\frac{\mathrm{d}(V_{\mathrm{a}}+V_{\mathrm{d}})}{\mathrm{d}u_{\mathrm{a}}}\frac{du_{\mathrm{a}}}{\mathrm{d}p}\right\} \tag{2}$$

where u_{w} and u_{a} are pore water pressure and pore gas pressure, respectively. u_{w} is the pore water pressure which is very close to the pore air pressure u_{a}. Eq. (2) can be re-arranged as below (Fredlund and Rahardjo, 1993):

$$C_{\mathrm{aw}} = -\left[\frac{V_{\mathrm{w}}}{V_{\mathrm{a}}+V_{\mathrm{w}}}\frac{1}{V_{\mathrm{w}}}\frac{\mathrm{d}V_{\mathrm{w}}}{\mathrm{d}u_{\mathrm{w}}}\right]\frac{\mathrm{d}u_{\mathrm{w}}}{\mathrm{d}p} - \left\{\frac{V_{\mathrm{a}}+V_{\mathrm{d}}}{V_{\mathrm{a}}+V_{\mathrm{w}}}\frac{1}{V_{\mathrm{a}}+V_{\mathrm{d}}}\frac{\mathrm{d}\,(V_{\mathrm{a}}+V_{\mathrm{d}})}{\mathrm{d}u_{\mathrm{a}}}\right\}\frac{\mathrm{d}u_{\mathrm{a}}}{\mathrm{d}p} \tag{3}$$

According to Henry's law, $V_{\mathrm{d}} = h_0 V_{\mathrm{w}}$, where h_0 is the Henry's constant. One can thus get the expression for C_{aw} in terms of water compressibility $C_{\mathrm{w}}(=\frac{dV_{\mathrm{w}}}{V_{\mathrm{w}}du_{\mathrm{w}}})$ and air compressibility C_{a} $(=\frac{dV_{\mathrm{a}}}{V_{\mathrm{a}}du_{\mathrm{a}}})$ based on Eqs. (1) and (3):

$$C_{\mathrm{aw}} = S_{\mathrm{r}}C_{\mathrm{w}}\left(\frac{\mathrm{d}u_{\mathrm{w}}}{\mathrm{d}p}\right) + (1 - S_{\mathrm{r}} + h_0 S_{\mathrm{r}})C_{\mathrm{a}}\left(\frac{\mathrm{d}u_{\mathrm{a}}}{\mathrm{d}p}\right) \tag{4}$$

Eq. (4) is the general expression for compressibility of the gas-water mixtures, considering partial pressures of the different phases. In undrained triaxial compression, $\frac{\mathrm{d}u_{\mathrm{w}}}{\mathrm{d}p} = B_{\mathrm{w}}$ and $\frac{\mathrm{d}u_{\mathrm{a}}}{\mathrm{d}p} = B_{\mathrm{a}}$, where B_{w} is the pore water pressure coefficient and B_{a} is the pore air pressure coefficient; C_{a} is expressed as $\frac{1}{u_{\mathrm{a}}+p_{\mathrm{a}}}$ according to Boyle's law and p_{a} is the atmospheric pressure (101 kPa). Eq. (4) can thus be rewritten as:

$$C_{\mathrm{aw}} = S_{\mathrm{r}}C_{\mathrm{w}}B_{\mathrm{w}} + (1 - S_{\mathrm{r}} + h_0 S_{\mathrm{r}})\frac{B_{\mathrm{a}}}{u_{\mathrm{a}} + p_{\mathrm{a}}} \tag{5}$$

For gassy sand with a relatively high degree of saturation, it is reasonable to assume u_{w}=u_{a} and $B_{\mathrm{a}} \approx B_{\mathrm{w}} \approx 1$ (Fredlund & Rahardjo, 1993). Eq. (5) can thus be simplified as:

$$C_{\mathrm{aw}} = S_{\mathrm{r}}C_{\mathrm{w}} + (1 - S_{\mathrm{r}} + h_0 S_{\mathrm{r}})\frac{1}{u_{\mathrm{a}} + p_{\mathrm{a}}} \tag{6}$$

The bulk modulus of the gas-water mixture K_{aw} is the reciprocal of C_{aw}

$$K_{aw} = \frac{1}{C_{\mathrm{aw}}} = \frac{1}{\frac{S_{\mathrm{r}}}{K_{\mathrm{w}}} + \frac{(1 - S_{\mathrm{r}})}{K_{\mathrm{a}}}} \tag{7}$$

where K_{w} =2.16×10^9 Pa

$$K_{\mathrm{a}} = \frac{(1 - S_{\mathrm{r}})(u_{\mathrm{a}} + p_{\mathrm{a}})}{(1 - S_{\mathrm{r}} + h_0 S_{\mathrm{r}})} \tag{8}$$

Since K_{w} is very large and $u_{\mathrm{a}} \approx u_{\mathrm{w}}$ in gassy sand, Eq. (8) can be simplified as:

$$K_{\mathrm{aw}} = (u_{\mathrm{a}} + p_{\mathrm{a}})\frac{1}{(1 - S_{\mathrm{r}} + h_0 S_{\mathrm{r}})} \tag{9}$$

Eq. (9) is used in modelling the gassy sand behavior in this study.

2.2 Definition of effective stress

Following Biot (1941), the effective sress σ_{ij}' is taken as the difference between the total stress σ_{ij} and a fraction called the Biot coefficient η_b of the pore pressure u_{w}. According to the mixture theory, the effective stress of multi-phase porous media, such as gassy sand, can be described as follows (Borja & Koliji, 2009):

$$\sigma_{\mathrm{ij}}' = \sigma_{\mathrm{ij}} - \eta_b S_{\mathrm{r0}} u_{\mathrm{w}} \delta_{\mathrm{ij}} - \eta_b S_{\mathrm{a0}} u_{\mathrm{a}} \delta_{\mathrm{ij}} = \sigma_{\mathrm{ij}} - \left(1 - \frac{K_0}{K_{\mathrm{s}}}\right) S_{\mathrm{r0}} u_{\mathrm{w}} \delta_{\mathrm{ij}} - \left(1 - \frac{K_0}{K_{\mathrm{s}}}\right) S_{\mathrm{a0}} u_{\mathrm{a}} \delta_{\mathrm{ij}} \quad (10)$$

where S_{r0} and S_{a0} are the initial liquid saturation and gas saturation, respectively. K_0 denotes the bulk modulus of the solid matrix, and K_{s} is the intrinsic bulk modus of the solid grain material. Considering the pore water pressure u_{w} in a gassy sand is very close to pore gas pressure u_{a} (Sobkowicz & Morgenstern, 1984; Pietruszczak & Pande, 1965), and the sum of S_{r0} and S_{a0} is equal to the unity, Eq.10 can be re-arranged as follows:

$$\sigma_{\mathrm{ij}}' = \sigma_{\mathrm{ij}} - \left(1 - \frac{K_0}{K_{\mathrm{s}}}\right) u_{\mathrm{w}} \delta_{\mathrm{ij}} \quad (11)$$

The bulk modulus K_0 of sand for the range of initial states (p'=0-400 kPa and e=0.53-0.74) concerned in this study does not exceed 160 MPa, as can be calculated using Richard et al. (1970)'s equation(Eq. 12). On the other hand, the bulk modulus of the sand grain material is approximately 20×10^3 MPa (Gurevich, 2004). It can be readily deduced that the value of Biot coefficient ($\eta_b = 1 - \frac{K_0}{K_{\mathrm{s}}}$) may range between 0.992 and 0.996, which is approximately 1.0 for the gassy sands studied herein. Therefore, the conventional definition for effective stress (i.e., difference between total stress and pore water pressure) is adopted for modelling gassy sand in this study, and elsewhere (Sobkowicz & Morgenstern, 1984;

Pietruszczak & Pande, 1965; Gurevich, 2004).

2.3 Elastic behavior

The elastic shear modulus G of the coarse-grained soil is described using Richard et al. (1970)'s equation, which depends on soil state (i.e., void ratio e and effective mean stress p'), as follows (see also Li and Dafalias, 2000):

$$G = \Gamma \frac{(2.97 - e)^2}{1 + e} \sqrt{p' p_\mathrm{a}} \tag{12}$$

where Γ is a material constant and p_a denotes the atmospheric pressure. The elastic bulk modulus K is expressed as below in terms of G and Poisson's ratio ν.

$$K = G \frac{2(1 + \nu)}{3(1 - 2\nu)} \tag{13}$$

2.4 Yield function

The present model is developed based on the one in Li and Dafalias (2000), which employs a state-dependent dilatancy relation and plastic hardening law. The yield surface is a straight line in the p'-q space without a cap. A stress-ratio based yield surface is used in this model (Pietruszczak, 2010; Li and Dafalias, 2000; Huang et al., 2010; Yin et al., 2013), as follows:

$$f = q - \eta p' = 0 \tag{14}$$

where η denotes the stress ratio (q/p'). This yield function was proposed based on the observed yield mechanism of coarse-grained soil in light of the previous experimental studies (Poorooshasb et al. 1966 and 1967; Shi et al., 2020; Northcutt & Wijewickreme, 2013). Their experimental results revealed that the plastic strain of coarse-grained soil occurs when the imposed η exceeded the maximum stress ratio experienced by the soil during its loading history. On the other hand, shearing at a constant η with either increasing or decreasing p'

produced a relatively small plastic volumetric strain, before the occurrence of particle breakage at an extremely high confining stress. Despite the sole consideration of shear-induced yield mechanism considered in this proposed model, an extension of the model can be made with ease to include the compression-induced yield mechanism by adding a yield cap controlled by p' (Li, 2002; Li & Dafalias 2002). In the proposed model, the critical line in the e-p' space is described using a power relationship $e-\left(\frac{p'}{p_a}\right)^{\xi}$, as suggested by Li and Wang (1998). It was recently found that the critical state line can be better captured by considering the interlocking law (Jin et al., 2017). Moreover, it could be further improved by adopting an exponential expression, which can eliminate the possibility of a negative value of the critical void ratio at high stress levels (Yin et al., 2018). For simplicity, the influence of these two factors is not taken into account in the model proposed herein.

2.5 State-dependent dilatancy

For gassy marine sand, where the degree of saturation mostly exceeds 85%, the gas bubbles only change the compressibility of the pore fluid of sand. Under this circumstance, the effective stress principle still works for the soil (Pietruszczak & Pande, 1996; Grozic et al., 2005). Therefore, the traditional forms of dilatancy, plastic modulus and the associated material parameters for saturated sand can still be used for the gassy sand. The state-dependent dilatancy function proposed by Li & Dafalias (2000) is used in this study:

$$D=\frac{\mathrm{d}\varepsilon_{\mathrm{v}}^{\mathrm{p}}}{\mathrm{d}\varepsilon_{\mathrm{d}}^{\mathrm{p}}}=\frac{d_0}{M}\left(Me^{m\psi}-\eta\right) \tag{15}$$

where $\mathrm{d}\varepsilon_{\mathrm{v}}^{\mathrm{p}}$ and $\mathrm{d}\varepsilon_{\mathrm{d}}^{\mathrm{p}}$ are plastic volumetric and plastic deviatoric strain increments, respectively. M denotes stress ratio at the critical state. d_0 and m are two material constants. Inspection of the equation suggests that the dilatancy of sand depends on the difference of the current stress ratio η from a reference stress ratio $Me^{m\psi}$. $D > 0$ and $D < 0$ mean contractive and dilative behavior, respectively. This type of formulation allows one to capture the following key features of dilatancy of a sand subjected to shear (Li & Dafalias, 2000):

(1) At a loose state ($\psi > 0$), the sand exhibits a contractive behavior ($D > 0$), as η is always lower than $Me^{m\psi}$ when $\psi > 0$ (Li, 2002);

(2) At a dense state ($\psi < 0$), the sand could show either zero dilatancy when $\eta = Me^{m\psi}$ (upon phase transformation), or a dilative behavior ($D < 0$) if otherwise (Li, 2002);

(3) At the critical state, the dilatancy vanishes ($D = 0$) being irrespective of the initial state, because $\eta = M$ and $\psi = 0$;

(4) The equation can be recovered to the dilatancy function of the original Cam clay model (i.e., $D = M - \eta$), by setting the two material constants as $d_0 = M$ and $m = 0$.

2.6 State-dependent plastic modulus

The plastic modulus (K_p) is defined as the ratio between the deviatoric stress increment ($\mathrm{d}q$) and plastic shear strain increment ($\mathrm{d}\varepsilon_\mathrm{q}^\mathrm{p}$), and can be formulated as a function of state parameter (Li & Dafalias, 2000), as follows:

$$K_\mathrm{p} = \frac{\mathrm{d}q}{\mathrm{d}\varepsilon_\mathrm{d}^\mathrm{p}} = \frac{hGe^{n\psi}}{\eta}\left(Me^{-n\psi} - \eta\right) \tag{16}$$

where n is a material constant. The value of h was found to depend on void ratio e, following the linear relation below:

$$h = h_1 - h_2 e \tag{17}$$

where h_1 and h_2 are two material constants. Eq. (16) was modified from Wang et al. (1990)'s formulation for plastic modulus, by taking ψ-dependency into account, as suggested by Muir

Wood et al. (1994). This improvement has enabled unified modelling of both strain-hardening and strain softening behavior of relatively loose and dense sands, respectively. The equation suggests that the plastic modulus is controlled by the difference of current stress ratio η from a 'virtual' peak stress ratio $Me^{-n\psi}$, which keeps changing during the shearing of the soil (Li & Dafalias, 2000). With Eq. (17), the key following features associated with the plastic hardening behavior of sand in shear can be reproduced:

(1) For any given initial state, $K_{\mathrm{p}} = \infty$ at $\eta = 0$, which is consistent with the behavior of sand showing $\mathrm{d}\varepsilon_{\mathrm{q}}^{\mathrm{p}} = 0$ induced by a tiny non-zero $\mathrm{d}\eta$ at $\eta = 0$ (Kuwano & Jardine, 2007);

(2) For any given initial state, $K_{\mathrm{p}} = 0$ at the critical state ($\eta = M$ and $\psi = 0$), because the term $\mathrm{d}\eta/\mathrm{d}\varepsilon_{\mathrm{q}}^{\mathrm{p}}$ (as defined in Eq. (16)) becomes zero;

(3) For a loose sand, $K_{\mathrm{p}} > 0$ (i.e., strain-hardening) during the entire process of shearing, because η is always smaller than $Me^{-n\psi}$;

(4) For a relatively dense sand, the formulation allows a smooth transition from $K_{\mathrm{p}} > 0$ (i.e., strain-hardening) to $K_{\mathrm{p}} < 0$ (i.e., strain-softening), when $\eta < Me^{-n\psi}$ and $\eta > Me^{-n\psi}$, respectively.

2.7 Constitutive equation for gassy sand

Based on this model and the compressibility of pore fluid (Eq. 9), the constitutive equation for a quasi-saturated gassy sand can be obtained as below:

$$\begin{Bmatrix} \mathrm{d}q \\ \mathrm{d}p' \\ \mathrm{d}u_w \end{Bmatrix} = \left\{ \begin{pmatrix} 3G & 0 & 0 \\ 0 & K & 0 \\ 0 & 0 & \dfrac{1+e}{e}K_{aw} \end{pmatrix} - \begin{pmatrix} 9G^2X & -3KG\eta X & 0 \\ 3KGDX & -K^2\eta DX & 0 \\ 0 & 0 & 0 \end{pmatrix} \right\} \begin{Bmatrix} \mathrm{d}\varepsilon_d \\ \mathrm{d}\varepsilon_v^b + \mathrm{d}\varepsilon_v^{aw} \\ \mathrm{d}\varepsilon_v^{aw} \end{Bmatrix} \tag{18}$$

with

$$X = \frac{h(L)}{K_p + 3G - K\eta D} \tag{19}$$

$$L = \frac{3Gd\varepsilon_d - K\eta\left(\mathrm{d}\varepsilon_v^b + \mathrm{d}\varepsilon_v^{aw}\right)}{K_p + 3G - K\eta D} \tag{20}$$

where $h(L)$ is the Heaviside function with $h(L) = 1$ for $L > 0$ and $h(L) = 0$ otherwise. The total volumetric strain increment of the soil element consists of two components, namely $\mathrm{d}\varepsilon_v^b$ and $\mathrm{d}\varepsilon_v^{aw}$. The former ($\mathrm{d}\varepsilon_v^b$) is associated with the changing mass of the gas-fluid mixture (due to either flow discharge or intake) within the element, while the latter ($\mathrm{d}\varepsilon_v^{aw}$) is caused by the volume change of the gas-fluid mixture (either volumetric compression or extension) in the element.

In a globally undrained test, $\mathrm{d}\varepsilon_v^b = 0$ but $\mathrm{d}\varepsilon_v^{aw} \neq 0$. While in a globally drained test (e.g., 1D consolidation or drained triaxial compression test), $\mathrm{d}u_w = 0$, which makes $\mathrm{d}\varepsilon_v^{aw} = 0$ in this case.

It is worth noting that Eq. (18) is formulated based on the idea that undrained shearing of gassy sand is accompanied by volumetric strain increment, which will, in turn, affect the excess pore water pressure, effective stress and hence the elasto-plastic stiffness matrix. Along this line, the total volumetric strain increment of the soil element consists of two components, namely $\mathrm{d}\varepsilon_v^b$ and $\mathrm{d}\varepsilon_v^{aw}$ ($\mathrm{d}\varepsilon_v = \mathrm{d}\varepsilon_v^b + \mathrm{d}\varepsilon_v^{aw}$). The former ($\mathrm{d}\varepsilon_v^b$) is associated with the changing mass of the gas-fluid mixture due to either flow discharge or intake from the simulated element, while the latter ($\mathrm{d}\varepsilon_v^{aw}$) is caused by the volume change of the gas-fluid mixture (either volumetric compression or extension) within the element. In a globally undrained test, $\mathrm{d}\varepsilon_v^b = 0$ but $\mathrm{d}\varepsilon_v^{aw} \neq 0$. The soil element will behave as it were partially drained, with a smaller amplitude of excess pore water pressure than that of its saturated equivalent. While in a globally drained test, $\mathrm{d}u_w = 0$, which makes $\mathrm{d}\varepsilon_v^{aw} = 0$. For this case, the presence of gas does not play any role, and Eq. (21) recovers to the conventional elasto-plastic matrix of non-gassy sand.

$$\begin{Bmatrix} \mathrm{d}q \\ \mathrm{d}p' \\ \mathrm{d}u_w \end{Bmatrix} = \left\{ \begin{pmatrix} 3G & 0 & 0 \\ 0 & K & 0 \\ 0 & 0 & \dfrac{1+e}{e}(u_\mathrm{a}+p_\mathrm{a})\dfrac{1}{(1-S_\mathrm{r}+h_0S_\mathrm{r})} \end{pmatrix} - \begin{pmatrix} 9G^2\dfrac{h(L)}{K_p+3G-K\eta D} & -3KG\eta\dfrac{h(L)}{K_p+3G-K\eta D} & 0 \\ 3KGD\dfrac{h(L)}{K_p+3G-K\eta D} & -K^2\eta D\dfrac{h(L)}{K_p+3G-K\eta D} & 0 \\ 0 & 0 & 0 \end{pmatrix} \right\} \begin{Bmatrix} \mathrm{d}\varepsilon_d \\ \mathrm{d}\varepsilon_v^b + \mathrm{d}\varepsilon_v^{aw} \\ \mathrm{d}\varepsilon_v^{aw} \end{Bmatrix} \tag{21}$$

where h_0 is the Henry's coefficient. The magnitude of h_0 affects the stiffness of the air-water mixtures and thus governs the gas exsolution and the compressibility of pore fluid in the constitutive equation. h_0 values of carbon dioxide (CO_2) and methane (CH_4), which are typically found in marine sediments and often used in triaxial tests, are 0.86 and 0.033, respectively.

The proposed model consists of eleven parameters for sand, and one material constant relating to the solubility of gas, as summarized in Table 2. The constitutive model under multi-axial loading condition is given in the Appendix. One more parameter c which describes the critical state stress ratio variation with the Lode's angle is needed.

3. Model validation

Most of the model parameters can be determined following the procedure shown in Li and Dafalias (2000) on saturated sand. Only one parameter h_0 is needed for gassy sand. This value can be readily obtained from the literature for different gasses. To adequately verify the proposed state-dependent gassy sand model, published results on gassy sands with a broad range of initial states have been adopted for model validation. These include undrained triaxial compression tests on loose gassy Ottawa Sand (ASTM Graded) (He & Chu, 2014), loose and dense gassy Ottawa Sand (CT-109A) (Grozic et al., 2005) and dense gassy Baskarp sand (Rad et al., 1994). Note that the Ottawa sand in He & Chu (2014) and Grozic et al. (2005) have slightly different particle shape, D_{50} and maximum void ratio e_{max} (Table 1). Their critical state lines in the *e*-*p*' plane can be better represented using different equations (Table 1). All the model parameters are listed in Table 2.

These gassy specimens were charged with typical types of bio-gases, including methane (CH_4), nitrogen (N_2) and carbon dioxide (CO_2). In each gassy specimen, the gas is present in two forms, namely free gas and dissolved gas. The former causes unsaturation of the sand specimen ($S_{\mathrm{r0}} < 100\%$), while the latter causes the pore water to be fully saturated with gas ($\alpha = 100\%$). S_{r0} is the initial saturation of the sample. The symbol α denotes the degree of water-gas saturation, which is defined as a percentage of the amount of dissolved gas in the pore water with respect to the maximum amount of gas which can be dissolved at the given pressure and temperature (Rad et al., 1994).

In addition to the model validation, the proposed gassy sand model is further accessed by comparing its predictive capability with that of the existing gassy sand models, i.e., models proposed by Lü et al. (2018) and Grozic et al. (2005), which contain an equivalent or larger number of parameters than the model proposed herein, respectively.

3.1 Loose gassy Ottawa Sand (ASTM Graded) (He & Chu, 2014)

A series of triaxial tests have been carried on loose gassy Ottawa sand (ASTM Graded) by He & Chu (2014) to investigate the effect of gas bubbles on reducing the potential of static liquefaction of the sand. The experimental program includes five undrained triaxial compression tests, i.e., four N_2-charged gassy specimens (S_{r0} ranging between 94.5% and 99.2%) and one saturated specimen. Fig. 2 compares the measured effective stress paths of the gassy and saturated Ottawa sand (ASTM Graded), along with the predicted results by the proposed gassy sand model in this study. The figure also includes the predicted results by Lü et al. (2018)'s model, which consists of the same number of model parameters.

The experimental results show that all the loose specimens exhibit collapse behavior (i.e., static liquefaction) subjected to the undrained shearing. The experiments also reveal that the presence of gas has played a 'beneficial' role in reducing positive excess pore water pressure of the loose sand, leading to higher peak strength than that of the saturated specimen. The 'beneficial' role becomes more pronounced with increasing amount of gas (i.e., decreasing value of S_{r}). These observed trends for all the specimens have been captured by the gassy sand models proposed in this study and by Lü et al. (2018)'s model.

One important feature to be captured by the constitutive model is the slope of the initial portion of effective stress path, which implies the elasto-plasticity of the soil at the very early stage of shearing. For the saturated specimen, the tangent line of the initial portion of effective stress path is measured to stay perpendicular to the p'-axis, suggesting a non-plastic behavior ($\mathrm{d}p'$=0, causing $\mathrm{d}\varepsilon_{\mathrm{v}}^{\mathrm{e}} = 0$ and thus $\mathrm{d}\varepsilon_{\mathrm{v}}^{\mathrm{p}} = 0$) in response to undrained shearing by a small $\mathrm{d}\eta$ at $\eta = 0$. This has been reproduced by the model proposed herein, thanks to the adopted functional form of plastic modulus K_{p} (see Eq. 16) that predicts an infinite value of K_{p}, and hence non-plastic response at $\eta = 0$. On the other hand, Lü et al. (2018)'s model predicts the initial portion of effective stress path to bend towards the left ($\mathrm{d}p' < 0$), suggesting the occurrence of plastic strain ($\mathrm{d}\varepsilon_{\mathrm{v}}^{\mathrm{e}} < 0$ and thus $\mathrm{d}\varepsilon_{\mathrm{v}}^{\mathrm{p}} > 0$) due to a very small stress ratio change. This is associated with the K_{p} formulation in their model, which predicts a finite value of K_{p} at $\eta = 0$, and plastic deformation at the early stage of shearing. The discrepancy for the initial slope of effective stress path has led to cumulative errors in predicting the subsequent collapse behavior (including the values of q_{peak} and η_{peak}) at larger stress ratios by their model.

For each gassy specimen, the measured initial portion of the effective stress path bends towards the right ($\mathrm{d}p' > 0$), with the amplitude of $\mathrm{d}p'$ increasing with account of gas. This is because the undrained shearing of each gassy specimen should have produced positive total volumetric strains, causing the effective stress path to behave as it were partially drained and bend to the right in p'-q space. The proposed model in this study is found to reasonably predict the slope of initial effective stress path of all the gassy specimens. While Lü et al. (2018)'s model does not appear to properly reproduce the initial slope of effective stress path for the two gassy specimens with relatively high S_{r} (i.e., 99.2% and 98.1%), which is caused by the definition of K_{p} at $\eta = 0$ as discussed above.

Fig. 3 shows the comparison between the measured and predicted [with the models proposed herein and by Lü et al. (2018)] stress-strain relationships for the gassy and saturated Ottawa sand in loose states (ASTM Graded). As shown by the test data, the saturated loose sand exhibit a brittle strain-softening behavior, which is a typical response during static liquefaction. With more undissolved gas, the specimens exhibit less brittle response and larger peak and residual strength, suggesting the 'beneficial' effect of the gas bubbles on loose sand. The models proposed in this study and by Lü et al. (2018) have reasonably captured all these features, including the influence of gas on the peak strength, the subsequent strain-softening behavior and the residual strength.

Fig. 4 compares the measured and predicted excess pore water pressures of the loose specimens that have been discussed in Figs. 2 and 3. As illustrated, the models proposed in this study and by Lü et al. (2018) both correctly capture the effect of gas on excess pore water pressure in the loose specimens, i.e., increasing amount of gas has led to reduction in excess pore water pressure. Because both models have considered the joint effects of free and dissolved gas in increasing the compressibility of the pore fluid (i.e., gas-water mixture), which in turn suppresses the generation of excess pore water pressure during the shear-induced contraction of the loose material.

3.2 Loose and dense gassy Ottawa Sand (CT-109A) (Grozic et al., 2005)

Grozic et al. (2005) reported undrained triaxial compression test results and their model predictions on another batch of Ottawa Sand (CT-109A), which contained carbon dioxide (CO_2) and were prepared in loose and dense states. The physical properties and model parameters of this Ottawa sand is different from the Ottawa Sand (ASTM Graded) tested by He & Chu (2014), as summarized in Tables 1 and 2.

Fig. 5 shows the comparison between the measured and predicted effective stress paths for the loose and medium dense gassy specimens. The measured and predicted stress-strain relationships for these gassy specimens are compared in Fig. 6. In the two figures, the predicted results by the model proposed in this study and by Grozic et al. (2005)'s model are included for comparison. It can be seen from Fig. 5 that the measured collapse behavior (i.e., static liquefaction) of the loose gassy specimen is well reproduced both models. On the other hand, the measured effective stress path of the dense gassy specimen (showing phase transformation) is only reasonably predicted by the model proposed herein, while Grozic et al. (2005)'s model does not properly capture the initial slope and thus the subsequent trajectory of the effective stress path. It is also illustrated by Fig. 6 that the model proposed in this study yields better prediction for the gassy specimens in different states than Grozic et al. (2005)'s model, although the latter contains more parameters. This suggests the suitability of the functional forms of plastic modulus and stress-dilatancy adopted in the model proposed herein, for properly capturing the state-dependency of sand.

3.3 Dense gassy and saturated Baskarp sand (Rad et al., 1994)

The results of dense gassy and saturated Baskarp sand (i.e., a fine river sand) were reported by Rad et al. (1994). The test programme consists of undrained triaxial compression tests on gassy and saturated specimens, as well as drained triaxial compression tests on saturated specimens. The gassy specimens were charged with either methane (CH_4) or carbon dioxide (CO_2). Two types of gassy specimens were prepared, i.e., specimens having free gas and gas-saturated water ($S_{\mathrm{r0}} < 100\%$, $\alpha = 100\%$) and specimens containing gas-saturated water without free gas ($S_{\mathrm{r0}} < 100\%$, $\alpha = 100\%$).

Figs. 7 and 8 compare the measured and predicted results from the drained triaxial compression tests on four dense saturated specimens, which were prepared at different e and p'. The results predicted by the model proposed herein show reasonable agreements with the measured shear stress-strain relationships (see Fig. 7) and dilatancy (see Fig. 8) for all the four specimens. In particular, the proposed model captures the peak strength and dilatancy for the specimens having different initial states, suggesting its predictive capability for the state-dependency of sand.

Figs. 9 and 10 compare the model predictions and experimental data for saturated and gassy specimens subjected to undrained triaxial compression. All the specimens were prepared to the same initial states (e=0.592 and p'=50 kPa), with exception of the gassy specimen containing CH_4 (e=0.585 and p'=50 kPa). The proposed model captures the trends of the stress-strain relationships (Fig. 9) and excess pore water pressures (Fig. 10) for all the gassy and saturated specimens.Specifically, the proposed model has reproduced the 'detrimental' effect of gas on the dense sand, i.e., presence of CH_4 has led to much lower strength and stiffness (Fig. 9) and less significant negative excess pore water pressure (Fig. 10) in the gassy specimens than their saturated equivalent. The reproduction of this key feature is achieved by properly formulating the coupled processes of (a) shear-induced negative excess pore water pressure in the dense specimens, (b) gas dissolution from the pore water and (c) the evolving stiffness of the water-gas mixture due to the joint effect of reducing gas solution and increasing amount of free gas.All in all, it is the gas exsolution under changing averaged pore fluid pressure that modifies the volume changes and hence impact on the overall shear strength and stiffness in a coupled manner.

4. Parametric study investigating the effect of gas on sands with different initial states

4.1 Motivation and programme of the parametric study

Existing studies have mainly focused the 'beneficial' effect of gas on the mitigation of static liquefaction of loose sand (Pietruszczak & Pande, 1996; Pietruszczak et al., 2003; Grozic et al., 2005; He & Chu, 2014), with little attention paid to systematically quantification of the 'detrimental' effect of gas on medium dense and dense sand. A systematic of parametric study is therefore carried out, aiming to investigate the influence of initial degree of saturation (i.e., S_{r0}) on the undrained shear behavior of sand with different initial states. The model parameters for Baskarp sand (i.e., a natural river sand) is adopted in the parametric study.

The parametric study consists of 119 analyses, which consider wide ranges of the initial relative density ($10\% \le D_{r0} \le 90\%$) and initial degree of saturation ($85\% \le S_{r0} \le 100\%$). Despite the variations in S_{r0} and D_{r0}, a constant initial effective mean stress (i.e., p_0'=200 kPa) is adopted for each analysis. The most commonly encountered bio-gas, namely methane (CH_4), is adopted in the parametric study. The Henry's constants h_0 for CH_4 is taken as 0.034, considering an environmental temperature of 4°C that is common at the seabed.

4.2 Distinct responses of loose and dense sand to effect of S_{r0}

Figs. 11(a), 11(b) and 11(c) shows the effect of S_{r0} on the stress-strain relationship, effective stress path and change of void ratio for typical CH_4-charged loose specimens (initial $D_{r0} = 10\%$) subjected to undrained triaxial compression, respectively. The saturated loose specimen exhibits a clear strain softening behavior (Fig. 11(a)), due to the significant reduction of p_0' accompanying positive excess pore water pressure of the contractive material (Fig. 11(b)) subjected to constant volume shearing (i.e., *e*=constant, see Fig. 11(c)).The inclusion of gas into the loose sand has led to a less brittle stress-strain relationship, along with higher peak stress ratio, larger peak and residual strength than those of saturated sand (Figs. 11(a) and (b)). This 'beneficial' effect is associated with the increased compressibility of the pore fluid by the occluded gas, which induces a partially drained response (volumetric contraction, see Fig. 11(c)) to suppress the development of positive excess pore water pressure of the contractive material. Consequently, the effective mean stress of the loose gassy sand under undrained shearing has reduced less than that of a saturated sand with the same initial state, and thus exhibit an improved mechanical behavior, i.e., higher stiffness and strength. When $S_{r0} = 0.85$, the peak undrained strength of the gassy sand is nearly 2 times of that for the saturated soil.

Figs. 12(a), 12(b) and 12(c) illustrates the effect of S_{r0} on the stress-strain relationship, effective stress path and change of void ratio for typical CH_4-charged dense specimens (initial $D_{\mathrm{r0}} = 90\%$) experiencing undrained triaxial compression, respectively. Different from the case for loose sand, the dense gassy and saturated specimens all exhibit strain-hardening behavior during the undrained shear (Fig. 12(a)). The addition of gas has resulted in smaller peak deviatoric stress in the gassy specimens, as compared to the saturated one. The 'detrimental' effect is because of the increased compressibility by gas, which suppresses development of negative excess pore water pressure of the dilative material (Fig. 12(b)) along with the partially drained response (volumetric dilation, see Fig. 12(c)). This has led to smaller increase in effective mean stress during undrained shearing of the dense gassy sand than that of a saturated sand with the same initial state, causing a weakened mechanical behavior of the former, i.e., lower stiffness and strength.

The 'detrimental' effect of gas on the dense sand is more significant as the amount of gas increases (i.e., lower S_{r0}). When $S_{\mathrm{r0}} = 0.85$, the peak deviatoric stress of dense gassy sand is only 60% of that for the saturated one.

4.3 Effect of gas on sand with various initial states

Fig. 13 shows the undrained strength ($s_{\mathrm{u\_gas}}$) of gassy sand with different D_{r0} (between 10% and 90%) and S_{r0} (between 85% and 100%) subjected to undrained shearing. The value of $s_{\mathrm{u\_gas}}$ for each gassy specimen in Fig. 13 is normalized by the undrained strength of its saturated equivalent ($s_{\mathrm{u\_sat}}$). A $s_{\mathrm{u\_gas}}/s_{\mathrm{u\_sat}}$ ratio being smaller than the unity means the gas has played a 'detrimental' role, and vice versa. The presence of gas is shown to reduce the undrained strength of a dense sand ($D_{\mathrm{r0}} = 90\%$) by up to 40%, or increase the undrained strength of a loose sand ($D_{r0} = 10\%$) by up to 140%. For each given D_{r0}, the modification effect of the gas becomes more significant at lower S_{r0}. The possibility of presence of gas, and their effects on stability of the seabed and marine structures founded on gassy seabed should therefore be considered in design and construction.

5. Model implementation and finite element analyses of slope instability

Having formulated and verified the gassy sand model, as presented in the preceding sessions, it is then implemented into a finite element (FE) code to offer a numerical tool for simulating various engineering problems that are affected by gas- and state-dependency of sand. Implementation of the proposed gassy sand model into a FE code is briefly described. The simulative capability of the implemented model is then illustrated through a typical boundary value problem, i.e., slope destabilized by undrained loading at its crest. Particular attention is paid to examine the ‘beneficial’ and ‘detrimental’ effects of gas on the stability of relatively loose and dense sandy slopes, respectively.

5.1 Implementation of the proposed gassy sand model

The proposed gassy sand model was implemented into a commercial FE package ABAQUS (Hibbitt et al., 2016), through its user-defined material interface (i.e., UMAT). The explicit Euler method in conjunction with automatic sub-stepping and error control (Sloan, 1987; Zhao et al., 2005) is employed for stress integration. The large strain formulation, as proposed by Hughes and Winget (1980) (see also ABAQUS User Manual (Hibbitt et al., 2016)), is adopted in the stress integration scheme. The numerical implementation schemes largely follow those employed by Gao (2012) and Gao et al.(2020), where more details are provided. The implemented gassy sand model in ABAQUS was verified by comparing its predicted results against the various triaxial tests on gassy and saturated sands, as readily presented in Section 4.

5.2 Finite element analysis on destabilization of gassy and saturated slopes

A total of four finite element simulations were carried out, including two analyses on relative loose slopes (average $D_{\mathrm{r0}} = 30\%$ at the mid-depth of the slope) and two on relatively dense slopes (average $D_{\mathrm{r0}} = 60\%$ at the mid-depth of the slope). For each D_{r0}, two degrees of saturation are considered, i.e., a fully saturated case (S_{r0}=100%) and a gassy case (S_{r0}=95% at the mid-depth of the slope). For all the analyses, the water depth is fixed at an elevation of 10 m above the crest of the slope. By assuming the amount of substance of CH_4 is 3.5mol/m^3 of each depth, the distribution of S_{r0} with depth for each gassy slope case can be readily deduced based on Henry's and Boyle's laws. Fig. 14(b) shows the distribution of S_{r0} along the depth, with the average of S_{r0}=95% of the mid-depth of the slope. The distribution of initial degree of saturation (S_{r0}) with depth is calculated from Henry's and Boyle's laws. According to the ideal gas equation of state (i.e., Boyle's law), the relationship between the initial amount of gas and initial gas pressure and can be described using the following equation:

$$(V_{\mathrm{a0}} + V_{\mathrm{d0}})(u_{\mathrm{a0}} + p_{\mathrm{a}}) = n_{\mathrm{g}} R_{\mathrm{g}} T_{\mathrm{g}} \tag{22}$$

In Eq. (22), $(V_{\mathrm{a0}} + V_{\mathrm{d0}})$ is the initial total volume of gas, consisting of the volume of free gas (V_{a0}) and gas dissolved in water (V_{d0}). u_{a0} is the initial pore gas pressure, which is very close to the initial pore water pressure u_{w0}. p_{a} is the atmospheric pressure (101 kPa). n_{g} is the amount of substance of the gas (unit: mol). R_{g} is a universal gas constant equal to 8.314

J/(mol·K). T_{g} is the absolute temperature of the gas, which is assumed to remain constant during the entire analysis. According to Henry's law and the definition for degree of saturation, the total initial volume of gas $(V_{\mathrm{a0}}+V_{\mathrm{d0}})$ can be further extended as below (Fredlund & Rahardjo, 1993):

$$(V_{\mathrm{a0}}+V_{\mathrm{d0}})=(V_{\mathrm{a0}}+V_{\mathrm{w0}})(1-S_{\mathrm{r0}}+h_0S_{\mathrm{r0}})=eV_{\mathrm{s0}}(1-S_{\mathrm{r0}}+h_0S_{\mathrm{r0}}) \tag{23}$$

where V_{w0} and V_{s0} denote the initial volume of the pore water and of the soil particles, respectively. h_0 is the Henry's constant. Based on Boyle's (Eq. 22) and Henry's laws (Eq. 23), the initial degree of saturation S_{r0} at each given depth of the gassy sand slope can be derived as below:

$$S_{\mathrm{r0}}=\frac{1-\dfrac{n_{\mathrm{g}}R_{\mathrm{g}}T_{\mathrm{g}}}{eV_{\mathrm{s0}}(u_{\mathrm{a0}}+p_{\mathrm{a}})}}{1-h_0} \tag{24}$$

By assuming that the amount of substance of CH_4 is uniformly distributed throughout the entire gassy sandy slope (i.e., 3.5mol/m^3), the variation of S_{r0} with depth (i.e., due to increasing pore air pressure) below the crest of each gassy slope can be readily calculated using Eq. 24, as shown in Fig. 14(b).

Fig. 14(a) shows the finite element mesh and boundary conditions, which are the same for all the four analyses. As illustrated, the slope has an inclined angle of 30°, with a rigid footing (width=3 m) sitting on its crest. It is intended to fail the slope in each analysis by imposing an undrained loading to the footing, which is a typical approach for quantifying the stability of a slope (Pantelidis & Griffiths, 2011)

The mesh consists of 3600 eight-node plane strain quadrilateral, bilinear displacement, bilinear pore water pressure and reduced intergration elements i.e., CPE8RP elements). The lateral boundaries and the bottom boundary are constrained by roller and pinned supports, respectively. Pore water pressure (PWP) boundaries are applied to the top and the bottom of the mesh, with the magnitudes of PWP determined based on the hydro-static pressure distributions. The proposed gassy sand model is employed to describe the constitutive behavior of the sand, with the calibrated parameters of Ottawa sand (ASTM graded, see Table 1) adopted for each analysis. The permeability (k) for Ottawa sand, which depends on its void ratio (e), was calculated using the equation proposed by Fleshman (2012), i.e., $k = 0.55\frac{e^3}{1+e}$. Other model parameters of the sand are summarized in Table 2, as described in the preceding section (i.e., Section 3).

Each analysis consists of two main procedures: (I) equilibrium of the initial geostatic stress field for the sloping ground; (II) triggering of the slope instability by imposing a surface load at the slope crest. In procedure (I), iterations were rendered to ensure the initial geostatic stress field (which is unknown) is in equilibrium with the applied gravity and initial boundary conditions. The iteration was not ceased till the calculated deformation of the slope under the action of the given initial geo-static stress field, gravity and initial boundary conditions became small than 10^{-7} m. This was followed by procedure (II), where a uniformly distributed load was applied at a rigid footing on the slope crest to destabilize the slope. To demonstrate the effect of gas on the shear-induced pore water pressure and thus the slope instability, procedure (II) was performed under the undrained condition. The loading time for procedure (II) in each analysis is 20 sec, which was sufficiently short to result in an undrained loading process, as determined from trial numerical runs with different loading times.

5.3 Effect of gas on stability of sandy slope with different densities

Figs. 15(a) and 15(b) compare the contour of the deviatoric strain ($\varepsilon_{\mathrm{d}} = \sqrt{\frac{2}{3} e_{\mathrm{ij}} e_{\mathrm{ij}}}$, where e_{ij} is the deviatoric strain tensor) developed in the saturated and gassy loose sandy slopes, due to an undrained loading of 40 kPa applied at the slope crest. The displacement vectors resulted from the undrained loading are also included in the two figures.

It can be seen from Fig. 15(a) that the surcharge loading leads to the formation of a continuous sliding wedge (with substantial shear strain), which extends from the slope toe to the slope crest. Significant soil movement develops within the sliding lines, while the soil outside the sliding wedge remains nearly stationary. Both observations suggest the failure of the slope under the undrained surcharge loading. With the presence of gas in the loose sandy slope (see Fig. 16(b)), however, the sliding wedge has not been continuously formed under the given load. Meanwhile, smaller soil movement is developed in the gassy slope than that in the saturated one. The comparison between Figs. 15(a) and 15(b) suggests the 'beneficial' effect of the gas on improving the undrained stability of a relatively loose sandy slope.

To further elaborate the 'beneficial' effect of gas on the loose sandy slope, Fig. 16 compares the change of effective stress path of a typical element at the same position in the saturated and gassy slopes (see the inset of the figure) during the surcharge loading process. As illustrated, the selected soil element (element A) in the saturated sandy slope fails due to static liquefaction, with the final value of mean effective stress *p*' approaching zero. Comparatively, the soil element in the loose sandy slope containing gas (element B) behaves less contractive (as explained in Session 4.1), leading to a higher *p*' at failure and consequently larger undrained shear strength with improved slope stability.

Figs. 17(a) and 17(b) compare the contour of induced deviatoric shear strain ($\varepsilon_{\mathrm{d}} = \sqrt{\frac{2}{3} e_{\mathrm{ij}} e_{\mathrm{ij}}}$, where e_{ij} is the deviatoric strain tensor), together with the displacement vectors, in the saturated and gassy dense sandy slopes under an undrained loading of 1500 kPa at the slope crest. The comparison between Figs. 17(a) and 17(b) shows that under a given surcharge loading, the slope containing gas exhibits a larger extend of sliding wedge than the slope with no gas, suggesting a 'detrimental' effect of gas on the dense sandy slopes. Relatively large deviatoric shear strain is developed in both gassy and saturated slope, i.e., ε_{d} is up to 150%. The computation of such large strains in ABAQUS is achieved by activating the option named Nlgeom, which considers geometric nonlinearity and rotation of local material directions of each deforming element during every increment of computation. The effect of gas on dense sandy slope is further elaborated, by inspecting the effective stress path of a typical element at the same location within the sliding wedge of the saturated and gassy slope, as shown in Fig. 18. It is seen that the selected element in the dense sandy slope containing gas (element C) behaves less dilative than that in the slope with no gas (element D), as explained in Session 4.3. This has led to a smaller undrained shear strength and reduced Results of the comparative study, as presented above, suggest that despite the high degree of saturation (S_{r0}=95%), the presence of the little amount of gas may significantly affect the undrained stability of slope. Ignorance of its presence may mislead the results of seabed stability analyses.

Summary and Conclusions

This study presents a state-dependent model for coarse-grained gassy soil, which can give a unified description of gassy sand with different initial states and degrees of saturation. The key elements of the state-dependent model include: (a) pressure-dependent compressibility of the gas-water mixture considering compression and dissolution of gas, (b) state-dependent dilatancy and (c) state-dependent plastic modulus of sand. These have enabled the model to properly capture the coupled processes of shear-induced excess pore water pressure, the resulted gas dissolution or exsolution from the pore water, and the evolving stiffness of water-gas mixture with changing amounts of free and dissolved gas.

The model is validated against triaxial test results on three gassy sands having various initial states (including dense and loose states) and degrees of saturation ($0.8 \leq S_{r0} \leq 1.0$), with reasonable agreements between the test data and model prediction. Compared to existing models, the current model can give better prediction of the sand response under various loading conditions with fewer or the same number of parameters. With the proposed model, the following distinct features of gassy sand have been reproduced:

(a) For a dilative gassy sand (i.e., in a dense state) subjected to undrained shearing, the induced excess pore water pressure is less negative than its statured equivalent, due to the reduced stiffness of the gas-water mixture in the former. This effect is intensified by the cumulated negative pore water pressure, which causes gas exsolution and expansion to further de-saturate the sand. Consequently, the presence of gas in dense sand plays a 'detrimental' role in suppressing negative excess pore water pressure, which in turn weakening its mechanical behavior.

(b) For a contractive gassy sand (i.e., in a loose state) subjected to undrained shearing, the resulted excess pore water pressure is less positive than its statured equivalent, because of the reduced stiffness of the gas-water mixture in the former. Although this effect is partly suppressed by the cumulated positive pore water pressure, which causes gas solution and compression to increase the degree of saturation of the sand, gas in loose sand plays a 'beneficial' role in suppressing positive excess pore water pressure, and thus increases its resistance against static liquefaction.

Parametric studies of undrained triaxial compression were performed on a calibrated natural river sand (i.e., Baskarp sand) that cover a wide range of initial relative density ($D_{\mathrm{r0}} = 10\text{\textasciitilde}90\%$) and degree of saturation ($S_{\mathrm{r0}} = 85\text{\textasciitilde}100\%$). The presence of gas is shown to reduce the undrained shear strength of a dense sand ($D_{\mathrm{r0}} = 90\%$) by up to 40%, or increase the undrained strength of a loose sand ($D_{\mathrm{r0}} = 10\%$) by up to 140%. This has highlighted the importance of in-situ characterization of gas, and quantifying and their effects on the undrained capacity of offshore foundations on gassy seabed subjected to extreme environmental loading at a high rate (e.g., hurricane).

The proposed gassy sand model was implemented into a finite element code, which is readily available to simulate various boundary value problems related to gassy and saturated sandy seabed. Illustrative examples are presented to simulate and compare gassy and saturated sandy slopes destabilized by an undrained loading at the slope crest. The presence of gas was shown to or weaken or improve the undrained stability of the loose and dense sandy slopes, respectively.

Acknowledgements

The authors gratefully acknowledge the financial supports provided by National Key Research and Development Program (2018YFE0109500), National Natural Science

Foundation of China (51779221 and 51939010) and the Key Research and Development Program of Zhejiang Province (2018C03031) and Zhejiang Provincial Natural Science Foundation (LHZ20E090001）.

Appendix

6.1 Definitions

The stress and strain tensors used in the generalization are defined as follows:

Deviatoric stress

$$s_{ij} = \sigma'_{ij} - p'\delta_{ij} \tag{A-1}$$

where δ_{ij} = Kronecker delta.

Stress ratio tensor

$$r_{ij} = \frac{s_{ij}}{p'} \tag{A-2}$$

The r_{ij} possesses two nontrivial invariants: a stress ratio second invariants R and the Lode angle θ defined as follows:

$$R = \sqrt{\frac{3}{2} r_{ij} r_{ij}} \tag{A-3}$$

$$\theta = -\frac{1}{3}\sin^{-1}\left(\frac{9}{2}\frac{r_{ij} r_{jk} r_{kl}}{R^3}\right) \tag{A-4}$$

Mean effective stress

$$p' = \frac{1}{3}\sigma'_{ij}\delta_{ij} = \frac{1}{3}\sigma'_{ii} = \frac{1}{3}(\sigma'_{11} + \sigma'_{22} + \sigma'_{33}) \tag{A-5}$$

The scalar value of deviatoric stress q (used in the simplified version of the model for triaxial space), is defined by:

$$q = \sqrt{\frac{3}{2} s_{ij} s_{ij}} \tag{A-6}$$

Deviatoric strain increment

$$\mathrm{d}e_{\mathrm{ij}} = \mathrm{d}\varepsilon_{\mathrm{ij}} - \frac{1}{3}\mathrm{d}\varepsilon_{\mathrm{v}}\delta_{\mathrm{ij}} \tag{A-7}$$

Volumetric strain increment

$$\mathrm{d}\varepsilon_{\mathrm{v}} = \mathrm{d}\varepsilon_{\mathrm{ii}} = \mathrm{d}\varepsilon_{11} + \mathrm{d}\varepsilon_{22} + \mathrm{d}\varepsilon_{33} \tag{A-8}$$

The scalar value of deviatoric strain increment $\mathrm{d}\varepsilon_{\mathrm{d}}$ is defined by:

$$\mathrm{d}\varepsilon_{\mathrm{d}} = \sqrt{\frac{2}{3}\mathrm{d}e_{\mathrm{ij}}\mathrm{d}e_{\mathrm{ij}}} \tag{A-9}$$

6.2 Generalization

With the stress and strain tensors defined above, the proposed model can be generalized for the multi-axial stress space, as follows:

6.2.1 Yield function

$$f = q - Hg(\theta)p' = 0 \tag{A-10}$$

where H is a hardening parameter whose evolution law depends on the stress state and void ratio. $g(\theta)$ is an interpolation function based on the Lode angle θ of r_{ij} or s_{ij} as follows (Li and Dafalias, 2002):

$$g(\theta) = \frac{\sqrt{(1+c^2)^2 + 4c(1-c^2)\sin 3\theta} - (1+c^2)}{2(1-c)\sin 3\theta} \tag{A-11}$$

where $c = M_{\mathrm{e}}/M_{\mathrm{c}}$ is a material constant, defining the ratio of the critical stress ratio in triaxial extension, M_{e}, and triaxal compression, M_{c}.

6.2.2 Hardening law and plastic modulus

The generalized form of plastic modulus can be obtained:

$$K_{\mathrm{p}} = \frac{Gh}{R}\left[M_{\mathrm{c}} g(\theta) e^{-n\psi} - R\right] \tag{A-12}$$

with the known K_{p},The value of h was found to depend on void ratio e, following the linear relation in Eq.(15):

$$\psi = e - e_c = e - \left[e_\Gamma - \lambda_c \left(\frac{p'}{p_a}\right)^{\xi}\right] \tag{A-13}$$

Where e_Γ, λ_c, and ξ are material constants and $p_a(= 101\ \mathrm{kPa})$ is the atmospheric pressure. ψ is the state parameter, which represents the difference between the current void ratio and the critical void ratio at a given effective mean normal stress.

6.2.3 Flow rule and dilatancy equation

The plastic deviatoric strain increment $\mathrm{d}e_{\mathrm{ij}}^{\mathrm{p}}$ is expressed as:

$$\mathrm{d}e_{\mathrm{ij}}^{\mathrm{p}} = \langle L \rangle m_{\mathrm{ij}}, \text{ with } m_{\mathrm{ij}} = \frac{\frac{\partial f}{\partial r_{\mathrm{ij}}} - \frac{\partial f}{\partial r_{\mathrm{mn}}} \delta_{\mathrm{mn}} \frac{\delta_{\mathrm{ij}}}{3}}{\left\| \frac{\partial f}{\partial r_{\mathrm{ij}}} - \frac{\partial f}{\partial r_{\mathrm{mn}}} \delta_{\mathrm{mn}} \frac{\delta_{\mathrm{ij}}}{3} \right\|} \tag{A-14}$$

The plastic shear strain increment is expressed as:

$$\mathrm{d}\varepsilon_{\mathrm{d}}^{\mathrm{p}} = \sqrt{\frac{2}{3} \mathrm{d}e_{\mathrm{ij}}^{\mathrm{p}} \mathrm{d}e_{\mathrm{ij}}^{\mathrm{p}}} = \langle L \rangle \sqrt{\frac{2}{3} m_{\mathrm{ij}} m_{\mathrm{ij}}} = \langle L \rangle \sqrt{\frac{2}{3}} \tag{A-15}$$

The plastic volumetric strain increment can be expressed as follows:

$$\mathrm{d}\varepsilon_{\mathrm{v}}^{\mathrm{p}} = \mathrm{d}\varepsilon_{\mathrm{ii}}^{\mathrm{p}} = \langle L \rangle \sqrt{\frac{2}{3}} D \tag{A-16}$$

The total plastic strain increment $\mathrm{d}\varepsilon_{\mathrm{ij}}^{\mathrm{p}}$ can be obtained as below:

$$\mathrm{d}\varepsilon_{\mathrm{ij}}^{\mathrm{p}} = \mathrm{d}e_{\mathrm{ij}}^{\mathrm{p}} + \frac{1}{3} \mathrm{d}\varepsilon_{\mathrm{v}}^{\mathrm{p}} \delta_{\mathrm{ij}} = \langle L \rangle \left(m_{\mathrm{ij}} + \frac{1}{3}\sqrt{\frac{2}{3}} D \delta_{\mathrm{ij}}\right) = \langle L \rangle x_{\mathrm{ij}} \tag{A-17}$$

The state-dependent dilatancy function is expressed as:

$$D = \frac{\mathrm{d}\varepsilon_{\mathrm{v}}^{\mathrm{p}}}{\left|\mathrm{d}\varepsilon_{\mathrm{d}}^{\mathrm{p}}\right|} = \frac{\mathrm{d}\varepsilon_{\mathrm{ii}}^{\mathrm{p}}}{\sqrt{\frac{2}{3} \mathrm{d}e_{\mathrm{ij}}^{\mathrm{p}} \mathrm{d}e_{\mathrm{ij}}^{\mathrm{p}}}} = \frac{d_1}{M_{\mathrm{c}} g(\theta)} \left[M_{\mathrm{c}} g(\theta) e^{m\psi} - R\right] \tag{A-18}$$

where $\mathrm{d}\varepsilon_{\mathrm{v}}^{\mathrm{p}}$ and $\mathrm{d}\varepsilon_{\mathrm{d}}^{\mathrm{p}}$ are plastic volumetric and plastic deviatoric strains increments, respectively. M_{c} denotes the ratio of the critical stress ratio under triaxal compression. d_1 and

m are two material constants.

6.2.4 Loading index

The loading index L can be readily derived through standard elastoplasticity procedures, as follows:

$$\langle L\rangle = \frac{\frac{\partial f}{\partial \sigma'_{\mathrm{kl}}} C_{\mathrm{klij}} \mathrm{d}\varepsilon_{\mathrm{ij}}}{K_{\mathrm{p}} + \frac{\partial f}{\partial \sigma'_{\mathrm{ab}}} C_{\mathrm{abcd}} x_{\mathrm{cd}}} = \Pi_{\mathrm{ij}} \mathrm{d}\varepsilon_{\mathrm{ij}} \tag{A-19}$$

where C_{ijkl} is the elastic stiffness matrix expressed as:

$$C_{\mathrm{ijkl}} = (K - 2G/3)\delta_{ij}\delta_{kl} + G(\delta_{ki}\delta_{lj} + \delta_{li}\delta_{kj}) \tag{A-20}$$

where $\frac{\partial f}{\partial \sigma'_{\mathrm{ij}}}$ can be expressed as follows:

$$\frac{\partial f}{\partial \sigma'_{\mathrm{ij}}} = \frac{\partial f}{\partial r_{\mathrm{kl}}}\left(\frac{\delta_{\mathrm{ki}}\delta_{\mathrm{lj}}}{p'} - \frac{\sigma'_{\mathrm{kl}}\delta_{\mathrm{ij}}}{3p'^2}\right) \tag{A-21}$$

The generalized incremental elastoplastic relation can be derived as follows:

$$\begin{aligned} \mathrm{d}\sigma'_{\mathrm{ij}} = C_{\mathrm{ijkl}}\left(\mathrm{d}\varepsilon_{\mathrm{kl}} - \mathrm{d}\varepsilon^{\mathrm{p}}_{\mathrm{kl}}\right) = C_{\mathrm{ijkl}}(\mathrm{d}\varepsilon_{\mathrm{kl}} - \langle L\rangle x_{kl}) = \left(C_{\mathrm{ijkl}} - h(L) C_{\mathrm{ijab}} x_{ab} \Pi_{kl}\right)\mathrm{d}\varepsilon_{kl} \\ = D_{\mathrm{ijkl}} \mathrm{d}\varepsilon_{kl} \end{aligned} \tag{A-22}$$

where $h(L)$ is the Heaviside step function, with $h(L > 0) = 1$ and $h(L \leq 0) = 0$.

References

Amaratunga A, Grozic JL. On the undrained unloading behaviour of gassy sands. Canadian Geotechnical Journal 2009;6(11):1267-1276.

Atigh E, Byrne PM. Liquefaction flow of submarine slopes under partially undrained conditions: An effective stress approach. Canadian Geotechnical Journal, 2004;41(1):154-165.

Biot MA., Willis DG. The elastic coefficients of the theory of consolidation. Journal of Applied Mechanics 1957;24:594-601.

Borja RI, Koliji A. On the effective stress in unsaturated porous continua with double porosity. Journal of The Mechanics and Physics of Solids 2009;57 (8):1182-1193.

Chu, J, Leong WK, Loke WL, Wanatowski D. Instability of loose sand under drained conditions. Journal of Geotechnical and Geoenvironmental Engineering 2012;138(2):207-216.

Esrig MI, Kirby RC. Implications of gas content for predicting the stability of submarine slopes. Marine Geotechnology 1977;2(1-4):81-100.

Fleshman MS. Laboratory modeling of critical hydraulic conditions for the initiation of piping. Dissertations&Theses-Gradworks 2012;187(4):391-429.

Fredlund DG, Rahardjo H. Soil mechanics for unsaturated soils. New York: John Wiley & Sons; 1993.

Finno RJ, Gallant AP. Effects of Gas on Blast Densification Verification. Korean Geotechnical Society Awards Lecture 2016.

Gao ZW. Constitutive modeling of anisotropic behavior in geomaterials: the role of fabric. PhD thesis 2012, Hong Kong University of Science and Technology.

Gao Z, Hong Y, Wang L. Constitutive modelling of fine-grained gassy soil: a composite approach. International Journal for Numerical and Analytical Methods in Geomechanics 2020; in press.

Gao ZW, Lu DC, Du XL. Bearing capacity and failure mechanism of strip footings on anisotropic sand. Journal of Engineering Mechanics2020;146(8):04020081.

Grozic JL, Robertson PK, Morgenstern NR. The behaviour of loose gassy sand. Canadian Geotechnical Journal 1999;36(3):482-492.

Grozic JL, Imam SM, Robertson PK, Morgenstern NR. Constitutive modeling of gassy sand behaviour. Canadian Geotechnical Journal 2005;42(3):812-829.

Gurevich B. A simple derivation of the effective stress coefficient for seismic velocities in porous rocks. Geophysics, 2004;69(2):393-397.

He J, Chu J. Undrained responses of microbially desaturated sand under monotonic loading.

Journal of Geotechnical and Geoenvironmental Engineering 2014;140(5):04014003.

He J, Chu J, Liu H. Undrained shear strength of desaturated loose sand under monotonic shearing. Soils and Foundations 2014;54(4):910-916.

Hibbitt, Karlsson, Sorensen. Abaqus user's manual, version6.14. Providence, RI, USA: Hibbitt, Karlsson & Sorensen Inc 2016.

Hight DW, Leroueil S. Characterisation of soils for engineering purposes. Characterisation and engineering properies of natural soils 2003;255-362.

Hughes TJR, Winget J. Finite rotation effects in numerical integration of rate constitutive equations arising in large deformation analysis. International Journal for Numerical Methods in Engineering 1980;15:1862-1867.

Hong J, Xu M. DEM study on the undrained mechanical behavior of gassy sand. Acta Geotech 2020;1861-1133.

Hong Y, Wang LZ, Yang B. and Zhang JF. Stress-dilatancy behaviour of bubbled fine-grained sediments. Engineering Geology 2019a;260(3):105-196.

Hong Y, Zhang JF, Wang LZ, Liu T. On evolving size and shape of gas bubble in marine clay under multi-stage loadings: μCT characterization and cavity contraction analysis. Canadian Geotechnical Journal 2019b.

Hong Y, Wang LZ, Zhang JF, Gao ZW. Forthcoming. 3D elastoplastic model for fine-grained gassy soil considering the gas-dependent yield surface shape and stress-dilatancy. Journal of Engineering Mechanics 2020.

Hughes TJR, Winget J. Finite rotation effects in numerical integration of rate constitutive equations arising in large deformation analysis. International Journal for Numerical Methods in Engineering 1980;15:1862-1867.

Huang M, Lu X, Qian J. Non-coaxial elasto-plasticity model and bifurcation prediction of shear banding in sands. International Journal for Numerical and Analytical Methods in Geomechanics 2010;34(9):906-919.

Ishihara K. Liquefaction and flow failure during earthquakes. Geotechnique 1993;43(3):351-415.

Jaky J. The coefficient of earth pressure at-rest. Journal of Society of Hungarian Architects and Engineers 1944;355-358.

Jommi C, Muraro S, Trivellato E, Zwanenburg C. Experimental results on the influence of gas on the mechanical response of peats.Géotechnique2019;69(9):753-766.

Jin YF, Wu ZX, Yin ZY, Shen JS. Estimation of critical state-related formula in advanced constitutive modeling of granular material. Acta Geotechnica 2017;12(6): 1329-1351.

Kuwano R, Jardine RJ. A triaxial investigation of kinematic yielding in sand. Géotechnique 2007;57(7):563-579.

Li XS, Wang Y. Linear Representation of Steady-State Line for Sand. Journal of Geotechnical & Geoenvironmental Engineering 1998;124(12):1215-1217.

Li XS, Dafalias YF. Dilatancy for cohesionless soils. Géotechnique 2000;50(4):449-60.

Li, XS. A sand model with state-dependent dilatancy. Géotechnique 2002;52(3):173-186.

Li XS, Dafalias YF. Constitutive modeling of inherently anisotropic sand behavior. J Geotech Geoenviron Eng 2002;128:868-80.

Lü XL, Huang M, Andrade José E. Modeling the static liquefaction of unsaturated sand containing gas bubbles. Soils and Foundations; 2018.

Muir Wood D, Delkheir K, Liu DF. Strain softening and state parameter for sand modelling. Géotechnique 1994;44:335-339.

Northcutt S, Wijewickreme D. Effect of particle fabric on the coefficient of lateral earth pressure observed during onedimensional compression of sand. Canadian Geotechnical Journal 2013;50(5):457-466.

Pantelidis L, Griffiths D. Stability assessment of slopes using different factoring strategies. Journal of Geotechnical and Geoenvironmental Engineering 2011;138(9):1158-1160.

Poorooshasb HB, Holubec I, Sherbourne AN. Yielding and flow of sand in triaxial compression, Part I. Canadian Geotechnical Journal 1966;3:179-190.

Poorooshasb HB, Holubec I, Sherbourne AN. Yielding and flow of sand in triaxial compression, Part II. Canadian Geotechnical Journal 1967;4:376-397.

Pietruszczak S, Pande GN. On the mechanics of partially saturated soils. Computers and Geotechnics 1991;12(1):55-71.

Pietruszczak S, Pande GN. Constitutive relations for partially saturated soils containing gas inclusions. Journal of Geotechnical Engineering 1996;122 (1).

Pietruszczak S, Pande GN, Oulapour M. A hypothesis for mitigation of risk of liquefaction. Géotechnique 2003;53:833-838.

Pietruszczak S. Fundamentals of Plasticity in Geomechanics. CRC Press; 2010.

Puzrin AM, Tront J, Schmid A, Hughes JB. Engineered use of microbial gas production to decrease primary consolidation settlement in clayey soils. Géotechnique 2011;61(9):785-794.

Rad NS, Lunne T. Gas in soil. I: detection and η-profiling. Journal of Geotechnical Engineering 1994;120(4):697-715.

Rad NS, Vianna AJD, Berre T. Gas in soils. ii: effect of gas on undrained static and cyclic strength of sand. Journal of Geotechnical Engineering 1994;120(4):716-736.

Rebata-Landa V, Santamarina JC. Mechanical Effects of Biogenic Nitrogen Gas Bubbles in Soils. Journal of Geotechnical and Geoenvironmental Engineering 2012;138(2):128-137.

Richart FE, Hall JR, Woods RD. Vibrations of soils and foundations. Englewood Cliffs, New Jersey: Prentice-Hall Inc.; 1970.

Rowe RK, Mabrouk A. Three-dimensional analysis of unanticipated behavior of a deep excavation. Canadian Geotechnical Journal 2018, 55(11):1647-1656.

Sánchez M, Gai X, Carlos Santamarina JC. A constitutive mechanical model for gas hydrate bearing sediments incorporating inelastic mechanisms. Computers and Geotechnics 2017;84:28-46.

Shi XS, Nie JY, Zhao JD, Gao YF. A homogenization equation for the small strain stiffness of gap-graded granular materials. Computers and Geotechnics 2020;121:103440.

Sloan SW. Substepping schemes for the numerical integration of elastoplastic stress-strain relations. International Journal for Numerical Methods in Engineering 1987;24(5):893-911.

Sobkowicz JC, Morgenstern NR. The undrained equilibrium behaviour of gassy sediments. Canadian Geotechnical Journal 1984;21(3):439-448.

Stagg CL, Schoolmaster DR, Krauss KW, Cormier N, Conner WH. Causal mechanisms of soil organic matter decomposition: deconstructing salinity and flooding impacts in coastal wetlands. Ecology 2017;98(8):2003-2018.

Sultan N, Garziglia S. Mechanical behaviour of gas–charged fine sediments: model formulation and calibration. Géotechnique 2014;64(11):851-864.

Vega-Posada CA, Finno RJ, Zapata-Medina DG. Effect of gas on the mechanical behavior of medium-dense sands. Journal of Geotechnical and Geoenvironmental Engineering 2014;140(11):04014063.

Verdugo R, Ishihara K. The steady state of sandy soils. Soils Foundations 1996;36:81-91.

Wang ZL, Dafalias YF , Shen CK. Bounding Surface Hypoplasticity Model for Sand. Journal of Engineering Mechanics 1990;116(5):983-1001.

Weast RC, Astle MJ, Beyer WH. CRC Handbook of Chemistry and Physics .CRC Press, 1984.

Wheeler SJ. The stress-strain behaviour of soils containing gas bubbles. PhD thesis, Oxford University 1986.

Wheeler SJ. A conceptual model for soils containing large gas bubbles. Géotechnique 1988a; 38(3):389-397.

Wheeler SJ. The undrained shear strength of soils containing large gas bubbles. Géotechnique 1988b;38(3):399-413.

Yang J, Yin ZY, Laouafa F, Hicher PY. Analysis of suffusion in cohesionless soils with randomly distributed porosity and fines content. Computers and Geotechnics 2019;111:157-171.

Yin ZY, Wu ZX, Hicher PY. Modeling the monotonic and cyclic behavior of granular materials by an exponential constitutive function. Journal of Engineering Mechanics 2018;144(4):04018014.

Yin ZY, Xu Q, Hicher PY. A simple critical state based double-yield-surface model for clay behavior under complex loading. Acta Geotechnica 2013;8(5):509-523.

Zhang JF. Micro-structure characterization and constitutive behavior of fine-grained gassy soil: from experiment to modelling. Master's thesis 2020, Zhejiang University.

Zhao JD, Sheng DC, Rouainia M, Sloan SW. Explicit stress integration of complex soil models. Int. J. Numer. Anal. Methods Geomech 2005.29:1209-1229.

Nomenclature

B_a	pore air pressure coefficient	p	mean total stress
B_w	pore water pressure coefficient	p_a	atmospheric pressure
c	material constant	p'	mean effective stress
C_a	air compressibility	q	deviator stress
C_w	water compressibility	R	stress ratio second invariants
C_{aw}	compressibility of gas-water mixture	r_{ij}	stress ratio tensor
C_{ijkl}	elastic stiffness tensors	s_{ij}	deviatoric stress
d_0	dilatancy constant	S_r	degree of saturation
D	state-dependent dilatancy function	S_{r0}	degree of saturation at initial state
D_{r0}	relative density at initial state	s_{u_gas}	undrained strength of gassy sand
e	void ratio	s_{u_sat}	undrained strength of saturated sand
e_c	void ratio at critical state	u_a	pore air pressure
e_Γ	material constants	u_w	pore water pressure
f	yield function	V_a	volume of free air in pore water
G	pressure-dependent shear modulus	V_w	volume of pore water
$g(\theta)$	interpolation function based on the Lode angle	V_d	volume of air dissolved in pore water
H	hardening parameter	$d\varepsilon_d$	deviatoric strain increment
h	hardening variable	$d\varepsilon_v$	volumetric strain increment
h_0	Henry's constant	$d\varepsilon_v^{aw}$	volumetric strain increment of gas-fluid mixture
h_1	hardening constants	$d\varepsilon_d^p$	plastic deviatoric strains increments
h_2	hardening constants	σ'_{ij}	effective stress
K	bulk elastic modulus	δ_{ij}	Kronecker's delta
K_a	bulk modulus of gas	σ_a	total axial stress
K_w	bulk modulus of water	σ_r	total radial stress
K_{aw}	bulk modulus of the gas-water mixture	θ	Lode angle
K_p	plastic modulus	Γ	shear modulus constant
L	plastic multiplier	η	stress ratio
M	stress ratio at critical state	ψ	material state variable
M_e	critical stress ratio in triaxial extension	ν	Poisson's ratio
M_c	critical stress ratio in triaxal compression	α	degree of water-gas saturation
m	dilatancy constant	ξ	material constants
n	material constant	λ_c	material parameter determining critical state line

Caption of Tables

Table 1. Typical engineering properties of three sands

	Meaning of parameters	Parameter	Ottawa loose gassy sand* (He & Chu, 2014)	Ottawa loose and medium dense gassy sand (Grozic et al., 2005)	Baskarp dense gassy sand (Rad et al., 1994)
Description	---	---	Ottawa sand (ASTM graded)	Ottawa sand (CT-109A)	Baskarp sand
Grain shape	---	---	Round	Sub-rounded to round	---
Basic parameters	Mean particle size (mm)	D_{50}	0.4	0.34	---
	Specific gravity	G_s	2.65	2.65	2.65
	Maximum void ratio	e_{max}	0.80	0.82	0.898
	Minimum void ratio	e_{min}	0.50	0.50	0.534
	Permeability (m/s)*	k_0	5×10^{-5}	---	---

Note: The two Ottawa sands have slightly different properties.

* The void ratio dependent permeability for Ottawa sand was calculated using the equation proposed by Fleshman (2012), i.e., $k = 0.55\frac{e^3}{1+e}$

Table 2. Model parameters of three gassy sands

	Meaning of parameters	**Parameter**	**Ottawa loose gassy sand (He & Chu, 2014)**	**Ottawa loose and medium dense gassy sand (Grozic et al., 2005)**	**Baskarp dense gassy sand (Rad et al., 1994)**
Elastic parameters	Elastic modulus	G_0	50	50	125
	Poission's ratio	ν	0.25	0.25	0.05
Critical state parameters	Stress ratio at the critical state	M	1.22	1.5	1.4
	Intercept of CSL in $e-\left(\frac{p'}{p_a}\right)^{\xi}$ or $e-\ln p'$ plane	e_Γ	0.806	1.1	0.886
	Slope of CSL in $e-\left(\frac{p'}{p_a}\right)^{\xi}$ or $e-\ln p'$ plane	λ_c	0.04	0.062	0.04
		ξ	---	---	0.7
Dilatancy parameters	Parameters of dilatancy function	d_0	1.2	0.88	1.2
		m	3.5	3.5	3.5
Hardening parameters	Parameters of the hardening law	h_1	3.15	3.15	3.15
		h_2	3.05	3.05	3.05
		n	1.1	1.1	1.1

Note: The critical state lines of Ottawa sand (ASTM graded) and Ottawa sand (CT-109A) are found to be linear in the $e-\log p'$ plane.

Caption of Figures

Fig. 1. (a) Representative element of gassy sand; (b) Three-phase diagram of gassy sand considering gas compression and dissolution

Fig. 2. Comparison between the measured and predicted stress paths of loose gassy Ottawa sand (ASTM graded) in undrained triaxial compression (Data from He & Chu, 2014)

Fig. 3. Comparison between the measured and predicted stress-strain behavior of loose gassy Ottawa sand (ASTM graded) in undrained triaxial compression (Data from He & Chu, 2014)

Fig. 4. Comparison between the measured and predicted excess pore water pressure of loose gassy Ottawa sand (ASTM graded) in undrained triaxial compression (Data from He & Chu, 2014)

Fig. 5. Comparison between the measured and predicted stress paths of loose gassy Ottawa sand (CT-109A) in undrained triaxial compression (Data from Grozic et al., 2005)

Fig. 6. Comparison between the measured and predicted stress-strain behavior of loose gassy Ottawa sand (CT-109A) in undrained triaxial compression (Data from Grozic et al., 2005)

Fig. 7. Comparison between the measured and predicted stress-strain behavior of dense saturated Baskarp sand in drained triaxial compression (Data from Rad et al., 1994)

Fig. 8. Comparison between the measured and predicted volumetric strain of dense saturated Baskarp sand in drained triaxial compression (Data from Rad et al., 1994)

Fig. 9. Comparison between the measured and predicted stress-strain behavior of dense gassy Baskarp sand of different saturation in undrained triaxial compression (Data from Rad et al., 1994)

Fig. 10. Comparison between the measured and predicted excess pore water pressure of dense gassy Baskarp sand of different saturation in undrained triaxial compression (Data from Rad et al., 1994)

Fig. 11. 'Beneficial' effect of gas bubbles in undrained triaxial compression test for loose sand: (a) effective stress path; (b) stress-strain relationship; (c) change of void ratio

Fig. 12. 'Detrimental' effect of gas bubbles in undrained triaxial compression test for dense sand: (a) effective stress path; (b) stress-strain relationship; (c) change of void ratio

Fig. 13. The undrained shear strength (s_{u_gas}) of gassy sand with varying initial states and degrees of saturation

Fig. 14. (a) Finite element mesh and boundary conditions for a slope destabilized by surcharge at the crest; (b) Degree of saturation along the depth below the slope crest

Fig. 15. Contours of the shear strain and displacement vectors for loose sand: (a) Saturated sand; (b) Gassy sand

Fig. 16. Comparison of stress paths of saturated loose sand and gassy loose sand at a point in the shear zone

Fig. 17. Contours of the shear strain and displacement vectors for dense sand: (a) Saturated sand; (b) Gassy sand

Fig. 18. Comparison of stress paths of saturated dense sand and gassy dense sand at a point in shear zone

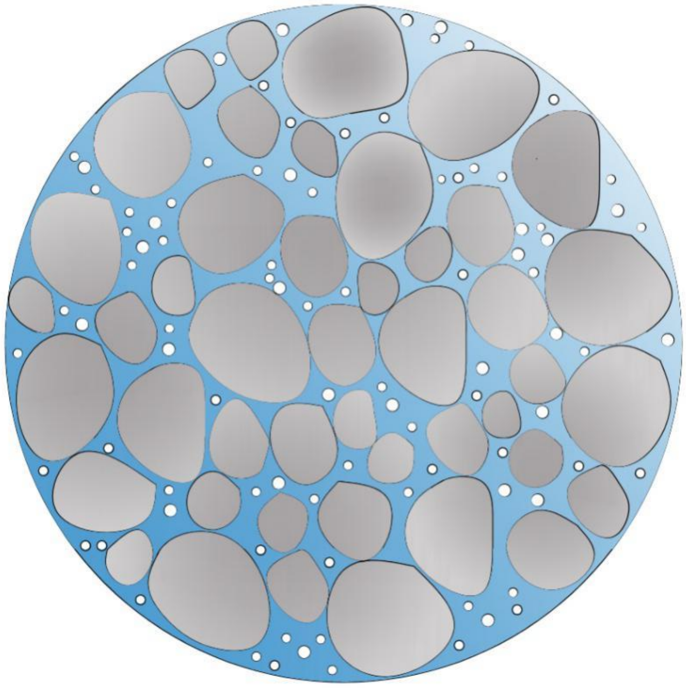

(a)

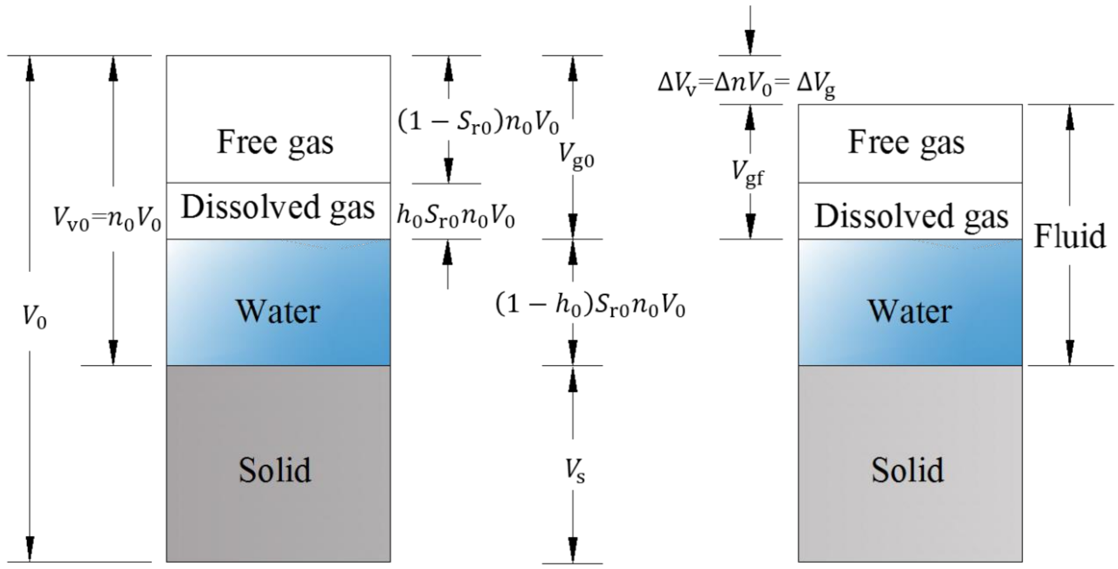

(b)

Fig. 1. (a) Representative element of gassy sand; (b) Three-phase diagram of gassy sand considering gas compression and dissolution

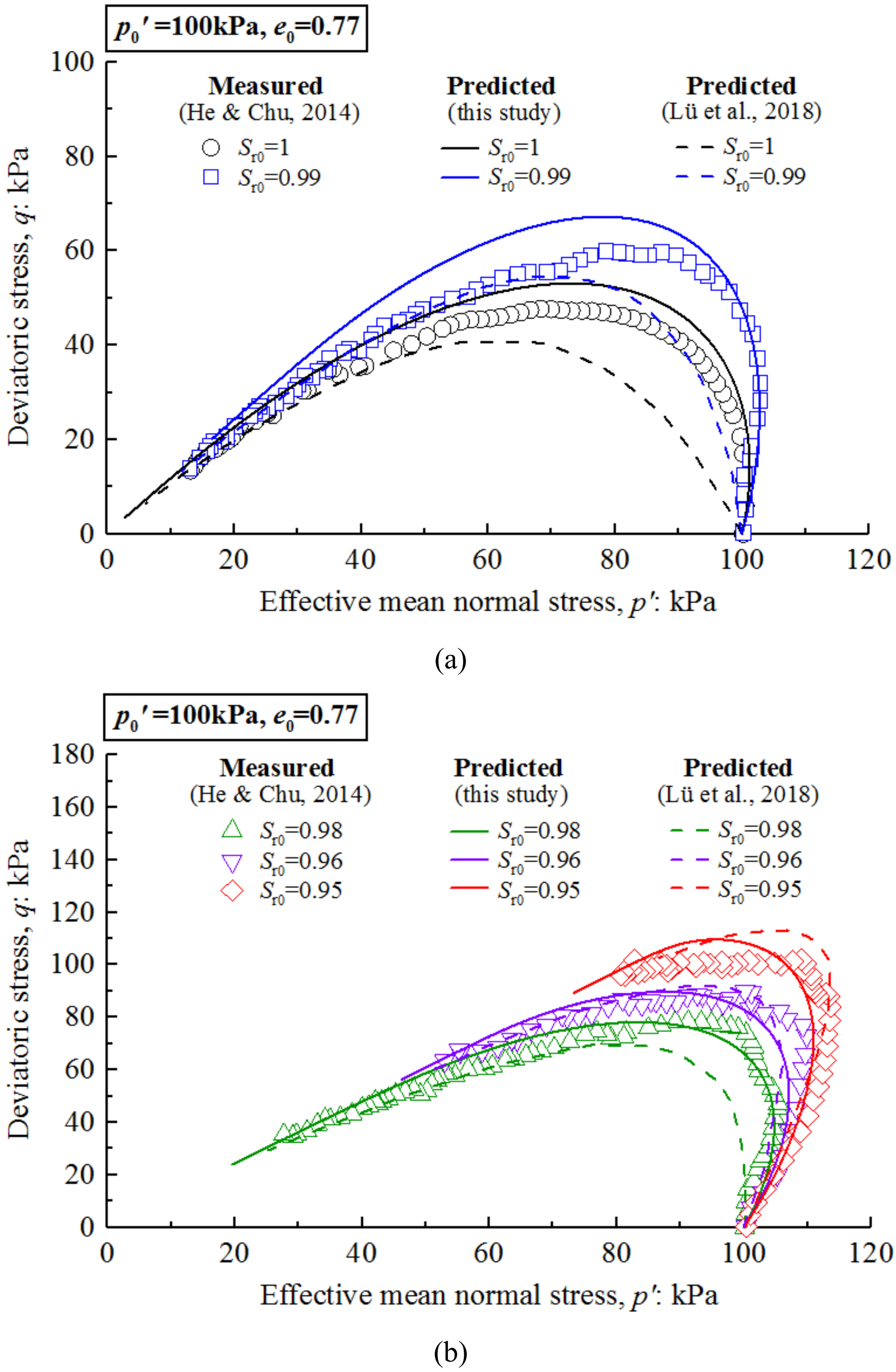

(b)

Fig. 2. Comparison between the measured and predicted stress paths of loose gassy Ottawa sand (ASTM graded) in undrained triaxial compression (Data from He & Chu, 2014)

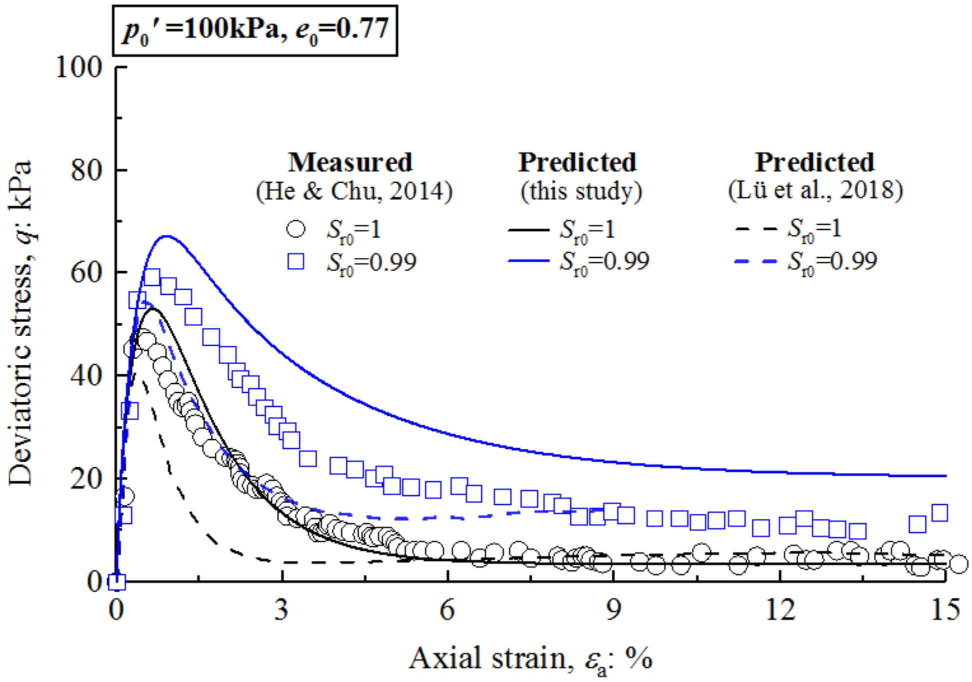

(a)

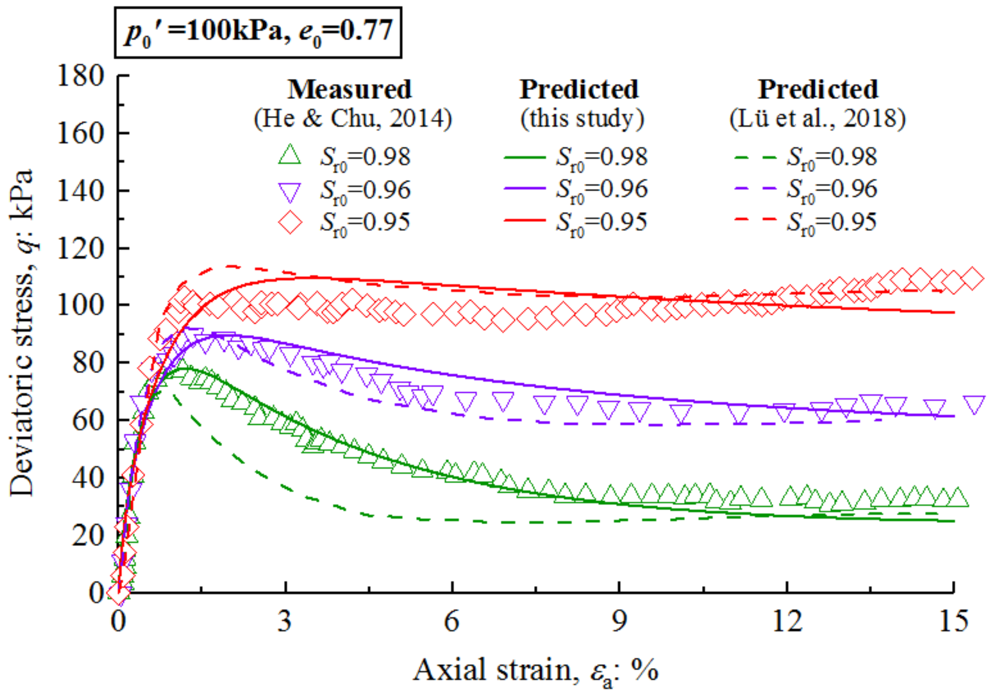

(b)

Fig. 3. Comparison between the measured and predicted stress-strain behavior of loose gassy Ottawa sand (ASTM graded) in undrained triaxial compression (Data from He & Chu, 2014)

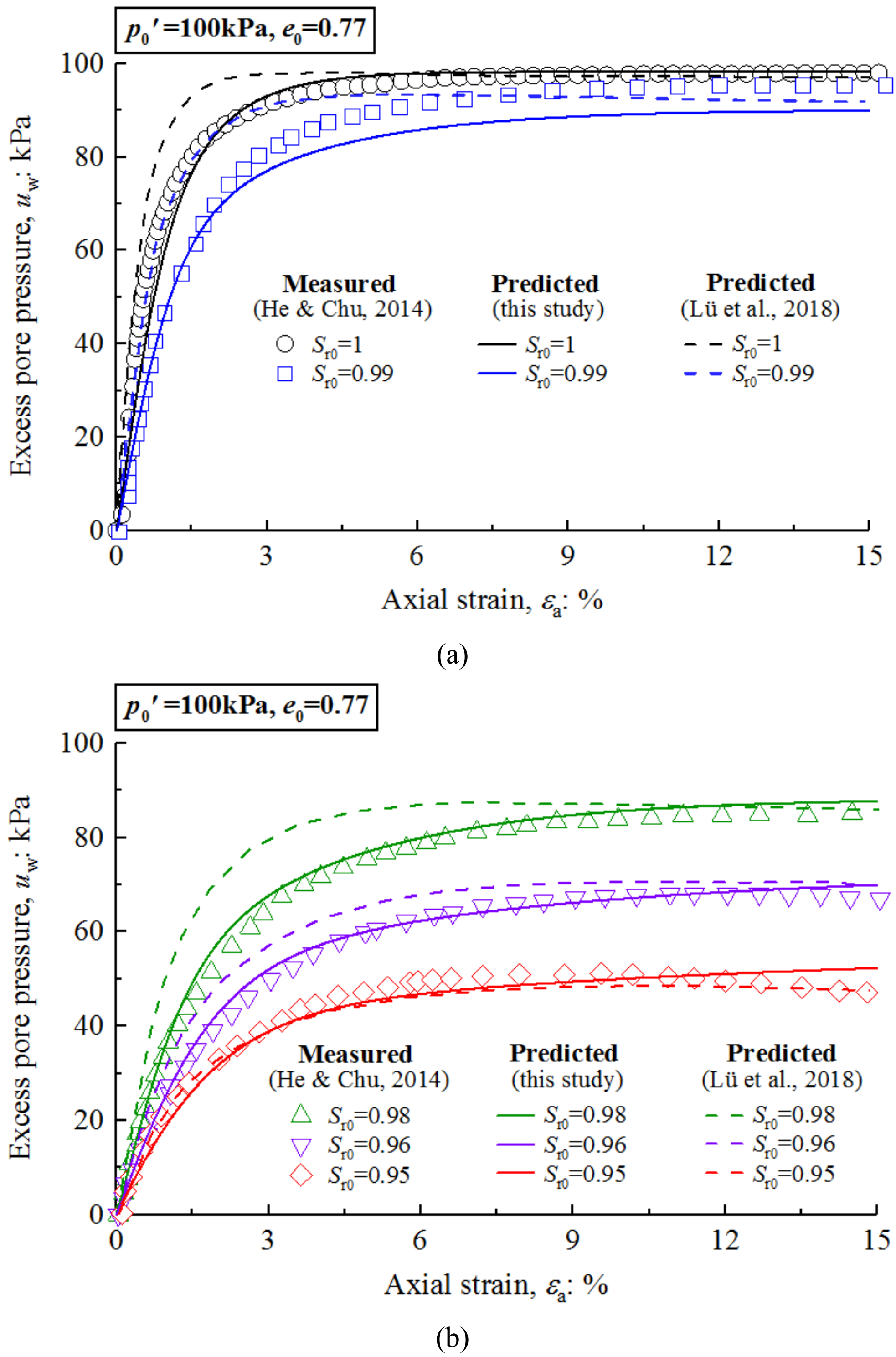

Fig. 4. Comparison between the measured and predicted excess pore water pressure of loose gassy Ottawa sand (ASTM graded) in undrained triaxial compression (Data from He & Chu, 2014)

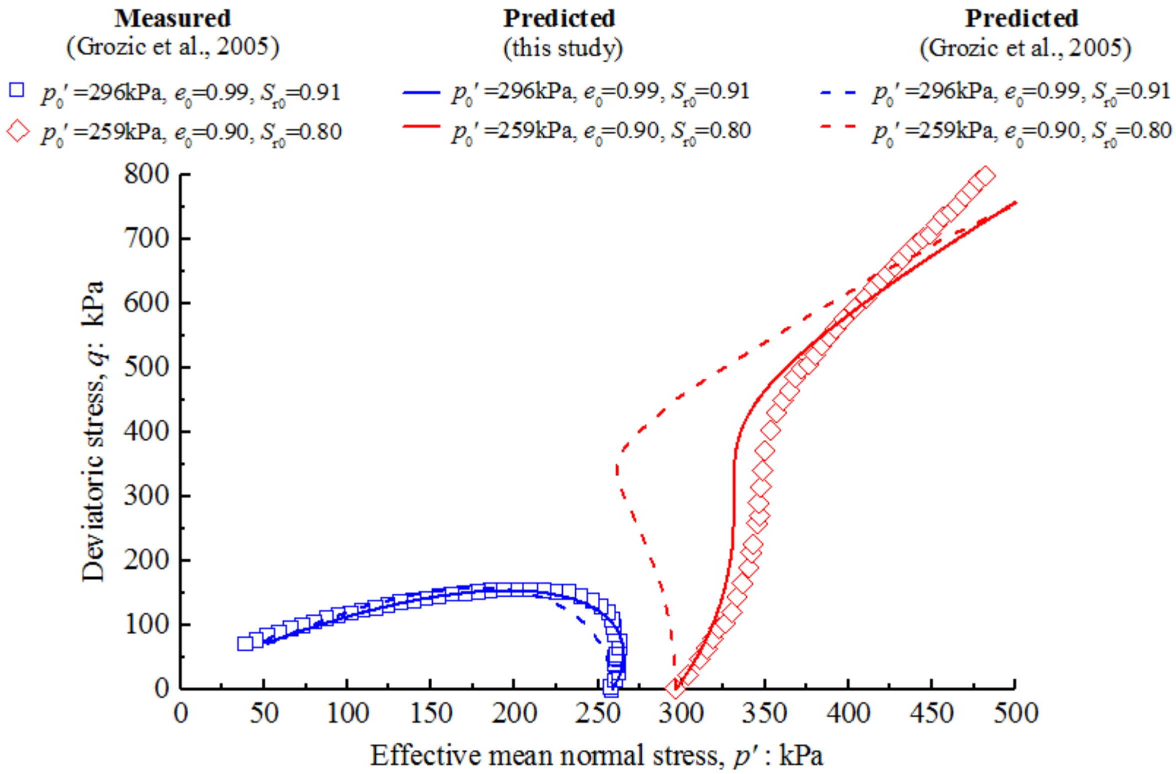

Fig. 5. Comparison between the measured and predicted stress paths of loose gassy Ottawa sand (CT-109A) in undrained triaxial compression (Data from Grozic et al., 2005)

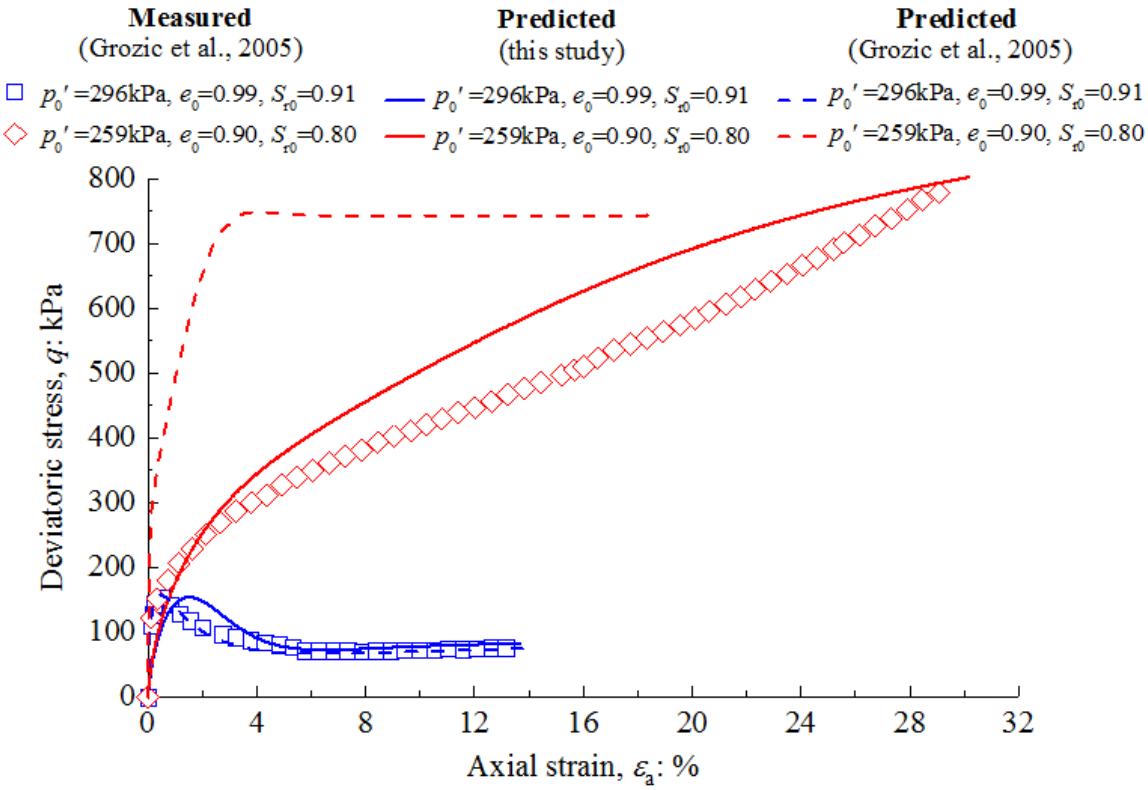

Fig. 6. Comparison between the measured and predicted stress-strain behavior of loose gassy Ottawa sand (CT-109A) in undrained triaxial compression (Data from Grozic et al., 2005)

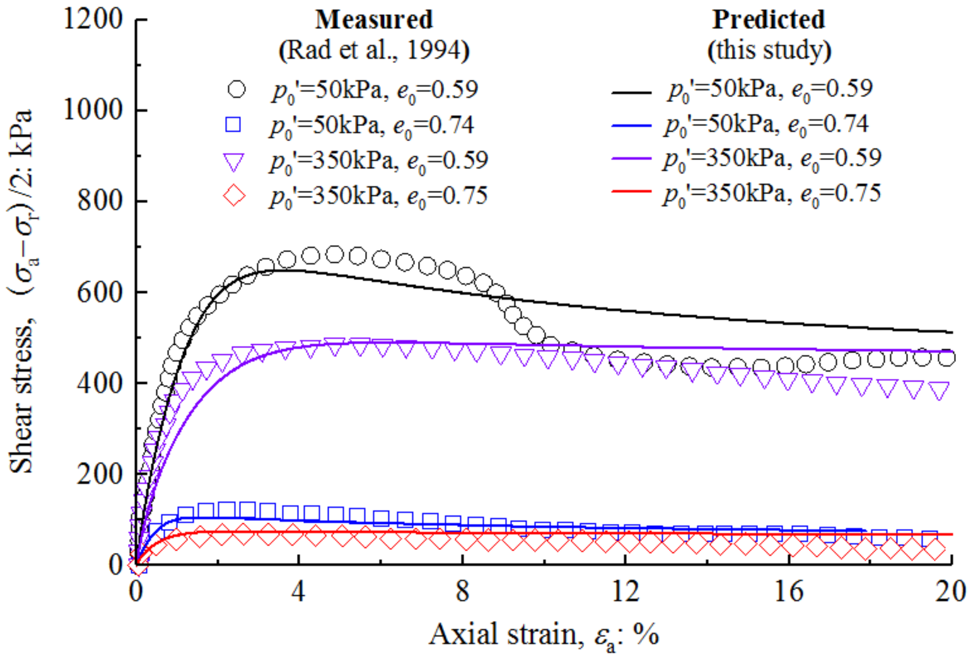

Fig. 7. Comparison between the measured and predicted stress-strain behavior of dense saturated Baskarp sand in drained triaxial compression (Data from Rad et al., 1994)

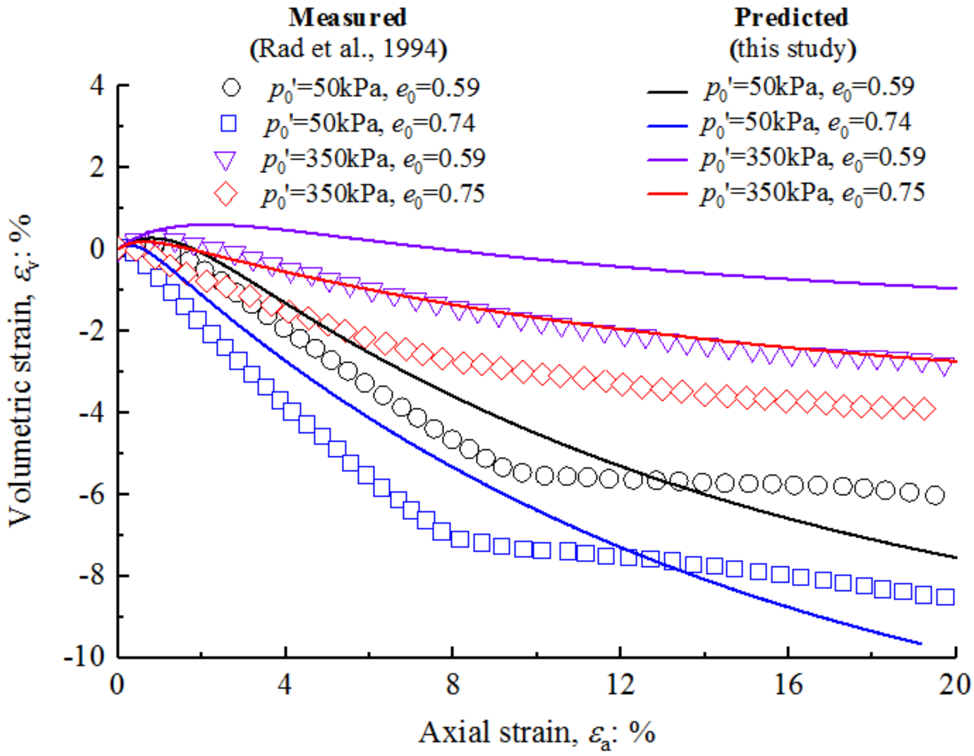

Fig. 8. Comparison between the measured and predicted volumetric strain of dense saturated Baskarp sand in drained triaxial compression (Data from Rad et al., 1994)

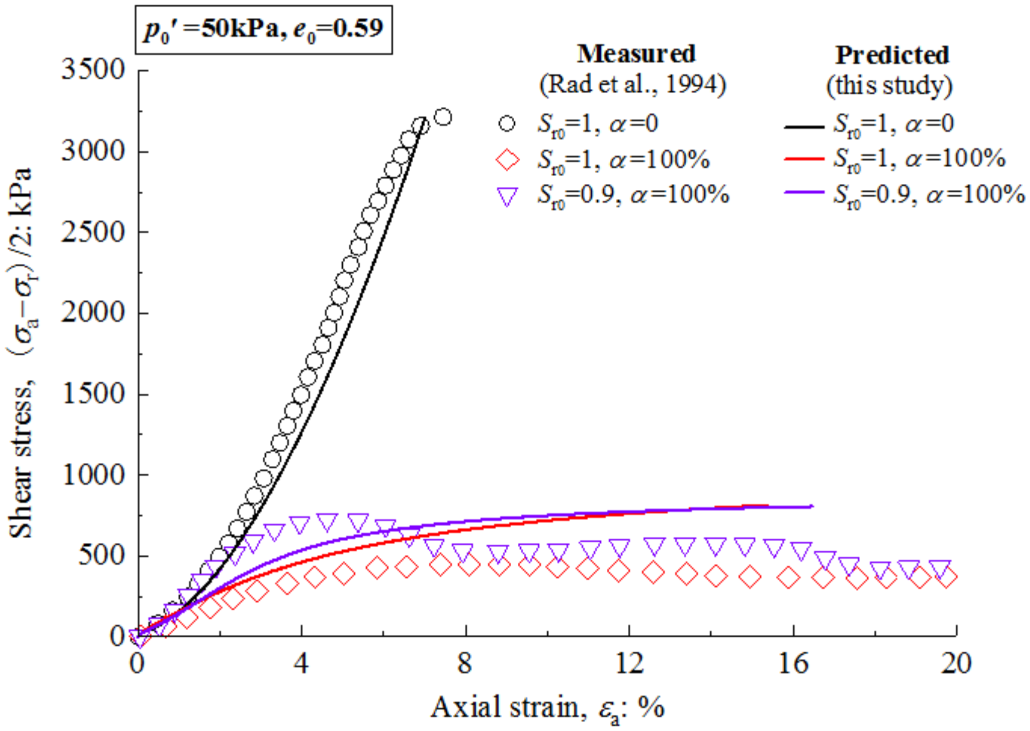

Note: α(degree of water-gas saturation) is defined as the amount of gas dissolved in the pore water divided by the maximum amount of gas that can be dissolved in the pore water.

Fig. 9. Comparison between the measured and predicted stress-strain behavior of dense gassy Baskarp sand of different saturation in undrained triaxial compression (Data from Rad et al., 1994)

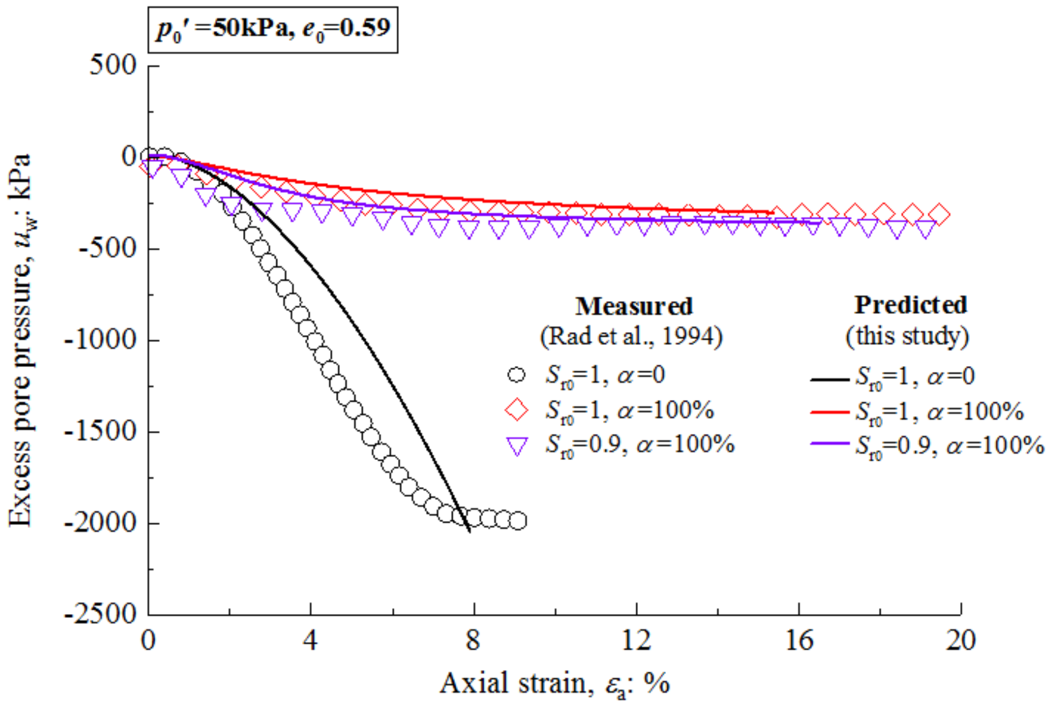

Note: α(degree of water-gas saturation) is defined as the amount of gas dissolved in the pore water divided by the maximum amount of gas that can be dissolved in the pore water.

Fig. 10. Comparison between the measured and predicted excess pore water pressure of dense gassy Baskarp sand of different saturation in undrained triaxial compression (Data from Rad et al., 1994)

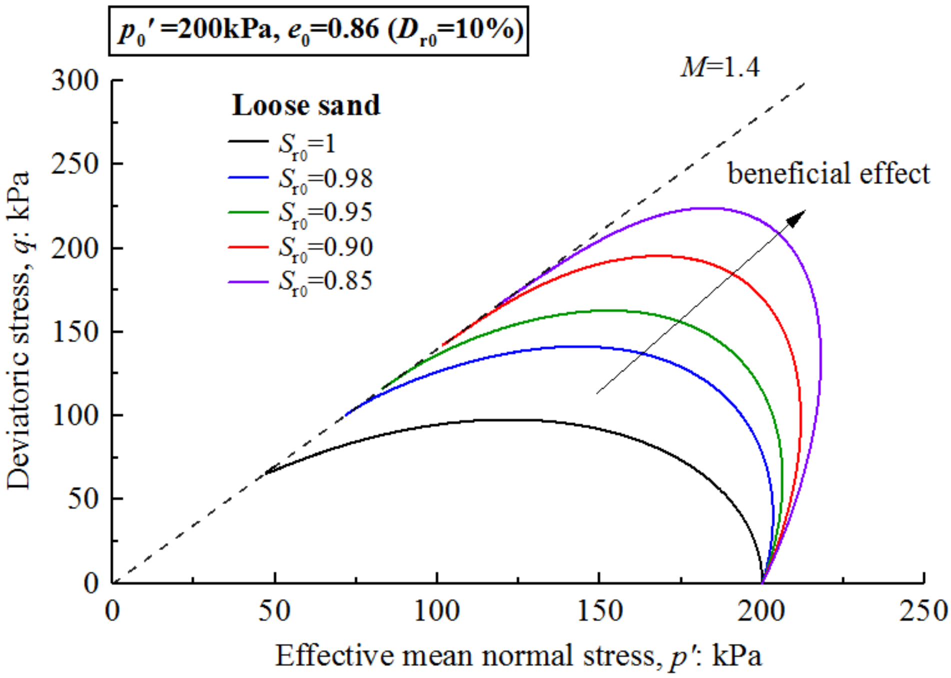

p0′ =200kPa, e0=0.86 (Dr0=10%)
M=1.4
Loose sand
Sr0=1
Sr0=0.98
Sr0=0.95
Sr0=0.90
Sr0=0.85
beneficial effect
300
250
200
150
100
50
0
Deviatoric stress, q: kPa
0
50
100
150
200
250
Effective mean normal stress, p′: kPa

(a)

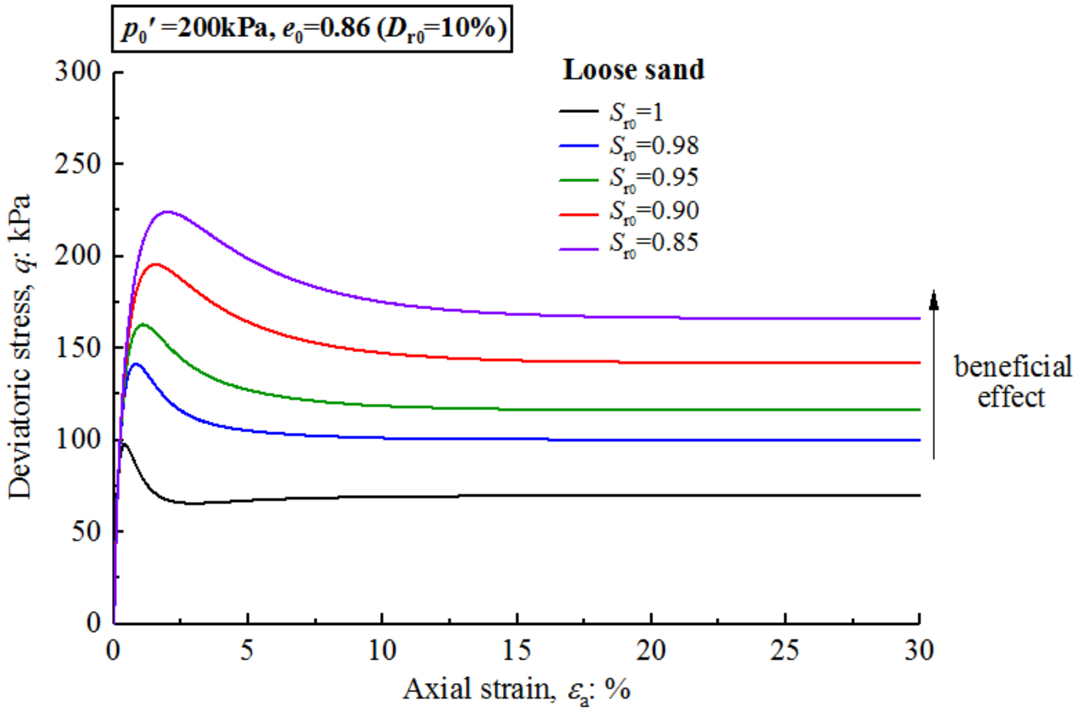

p0′ =200kPa, e0=0.86 (Dr0=10%)
Loose sand
Sr0=1
Sr0=0.98
Sr0=0.95
Sr0=0.90
Sr0=0.85
beneficial effect
300
250
200
150
100
50
0
Deviatoric stress, q: kPa
0
5
10
15
20
25
30
Axial strain, εa: %

(b)

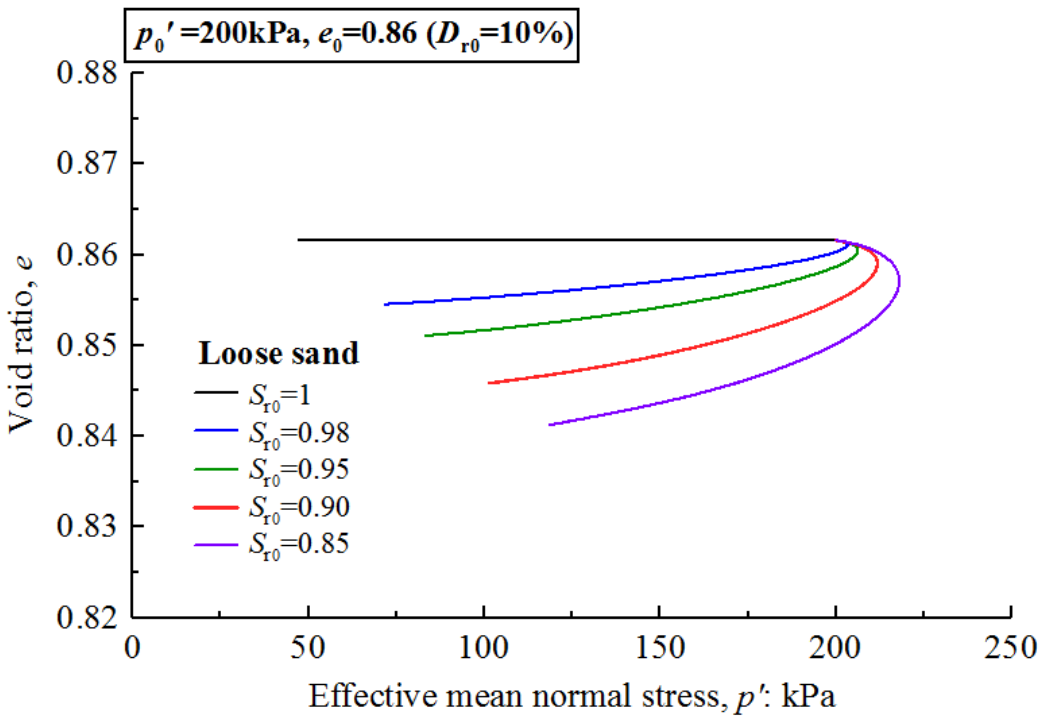

(c)

Fig. 11. 'Beneficial' effect of gas bubbles in undrained triaxial compression test for loose sand: (a) effective stress path; (b) stress-strain relationship; (c) change of void ratio

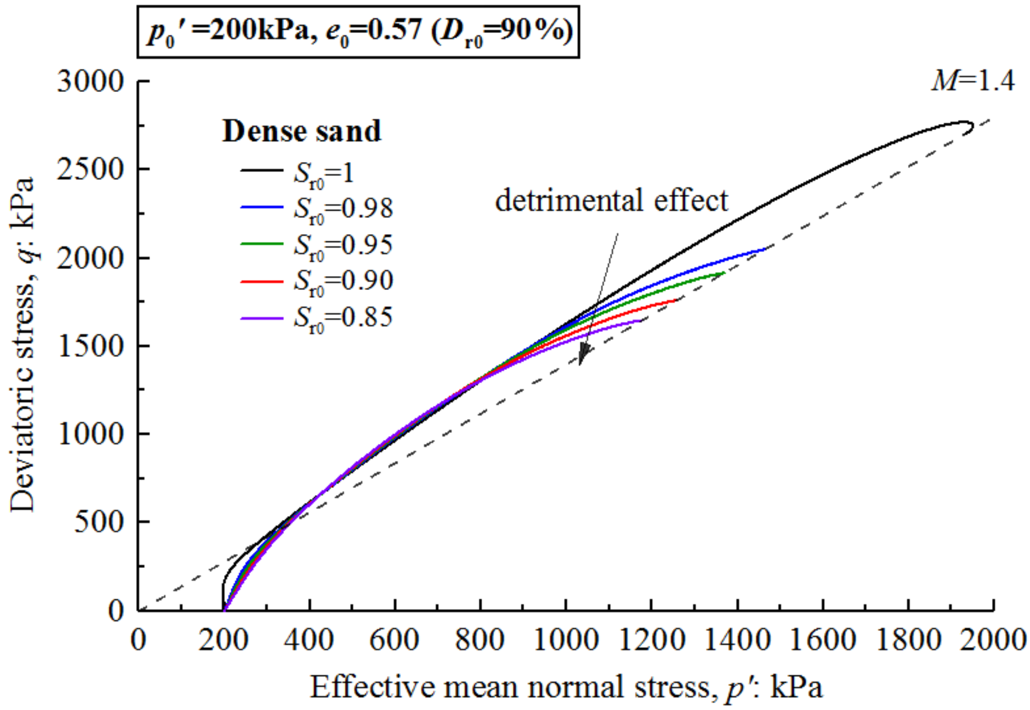

p_0' =200kPa, e_0=0.57 (D_{r0}=90%)
Dense sand
S_{r0}=1
S_{r0}=0.98
S_{r0}=0.95
S_{r0}=0.90
S_{r0}=0.85
M=1.4
detrimental effect
Deviatoric stress, q: kPa
Effective mean normal stress, p': kPa

(a)

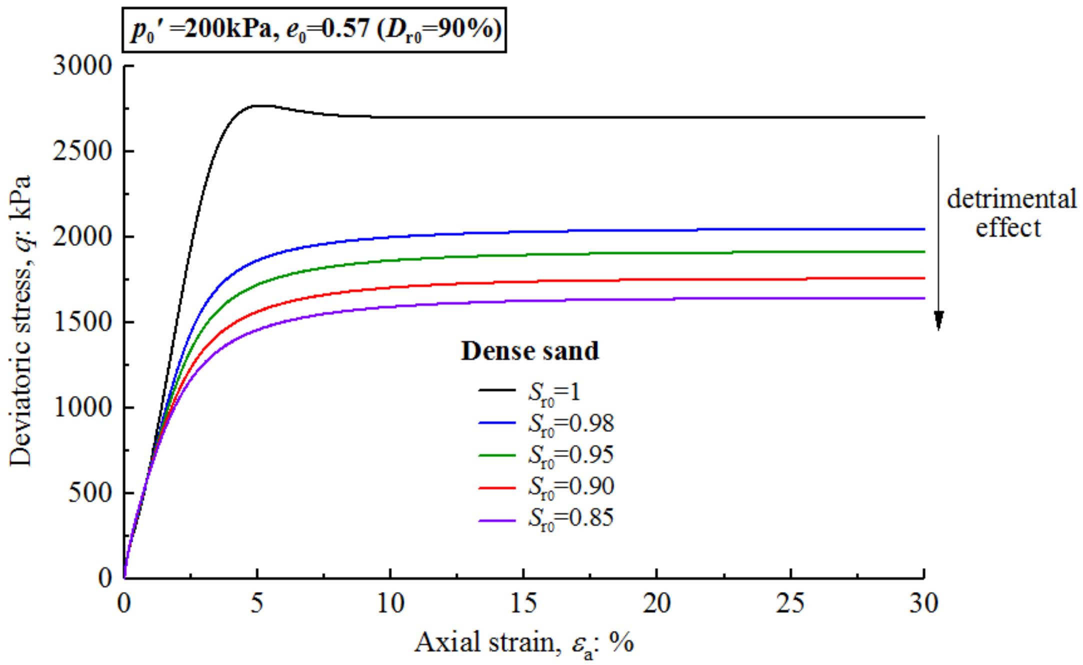

p_0' =200kPa, e_0=0.57 (D_{r0}=90%)
detrimental effect
Dense sand
S_{r0}=1
S_{r0}=0.98
S_{r0}=0.95
S_{r0}=0.90
S_{r0}=0.85
Deviatoric stress, q: kPa
Axial strain, ε_a: %

(b)

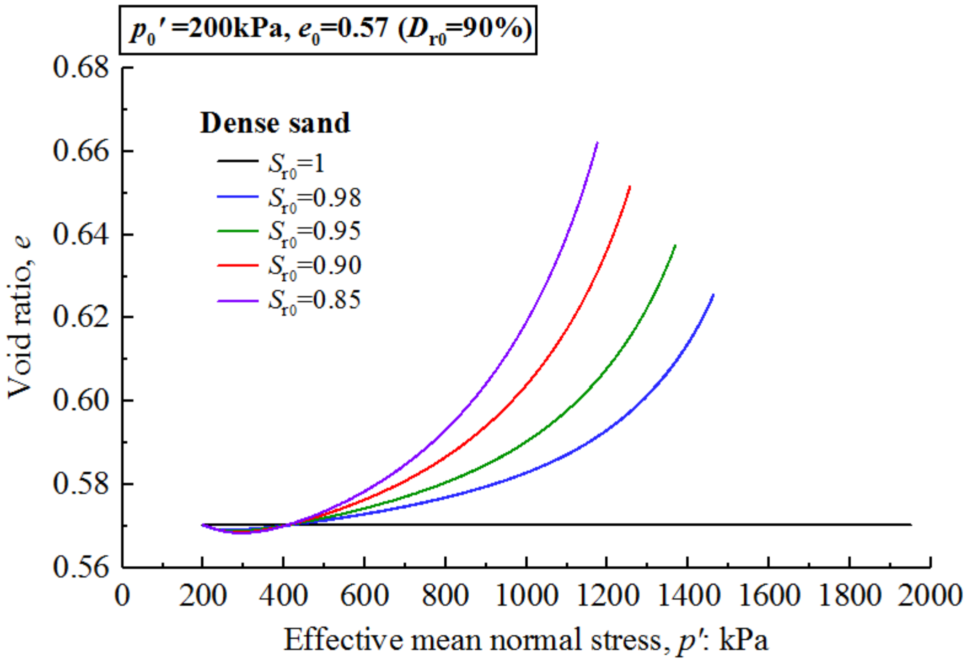

(c)

Fig. 12. 'Detrimental' effect of gas bubbles in undrained triaxial compression test for dense sand: (a) effective stress path; (b) stress-strain relationship; (c) change of void ratio

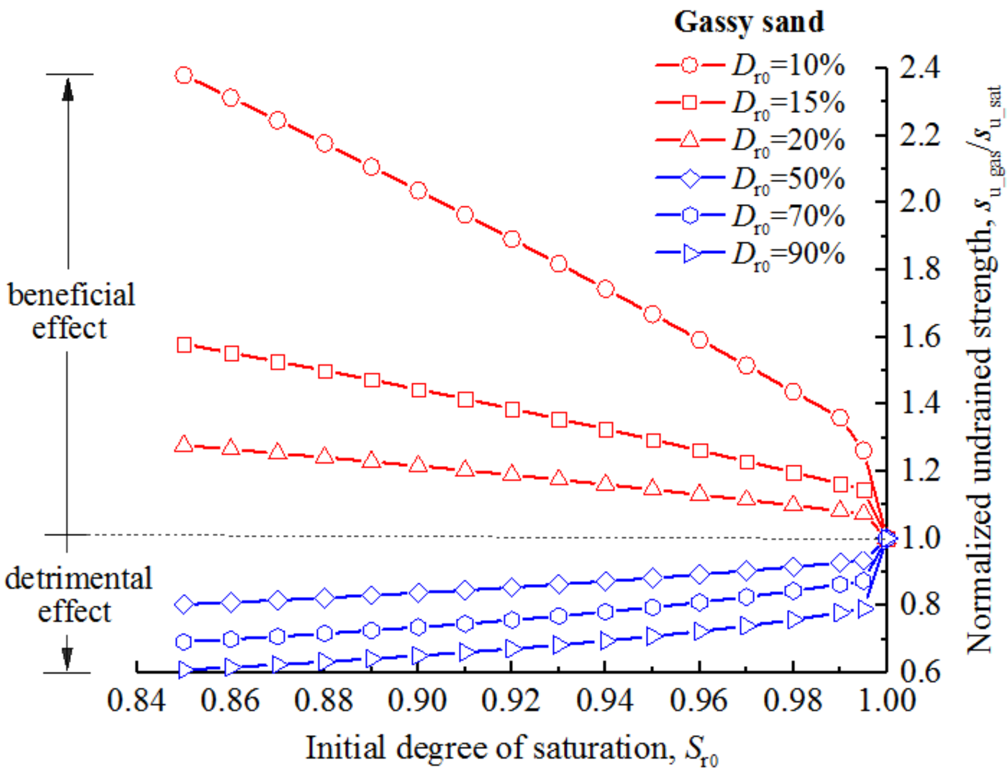

Fig. 13. The undrained shear strength (s_{u_gas}) of gassy sand with varying initial states and degrees of saturation

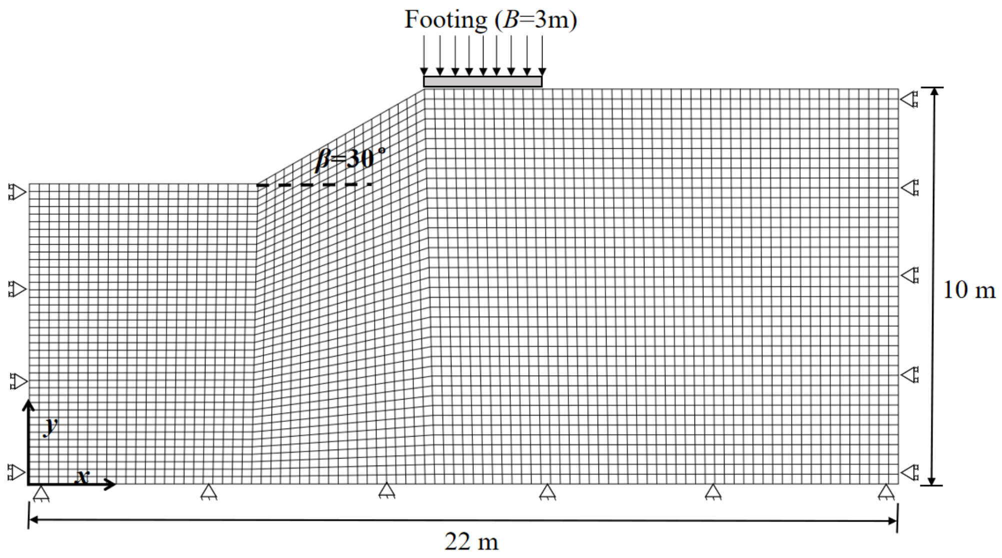

(a)

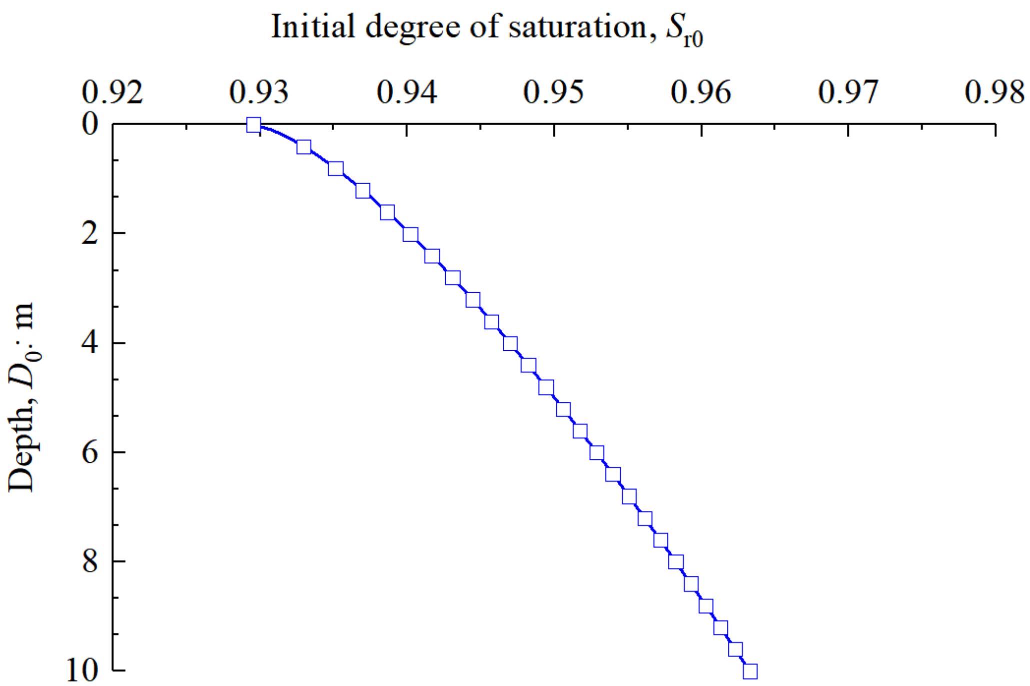

(b)

Fig. 14. (a) Finite element mesh and boundary conditions for a slope destabilized by surcharge at the crest; (b) Degree of saturation along the depth below the slope crest

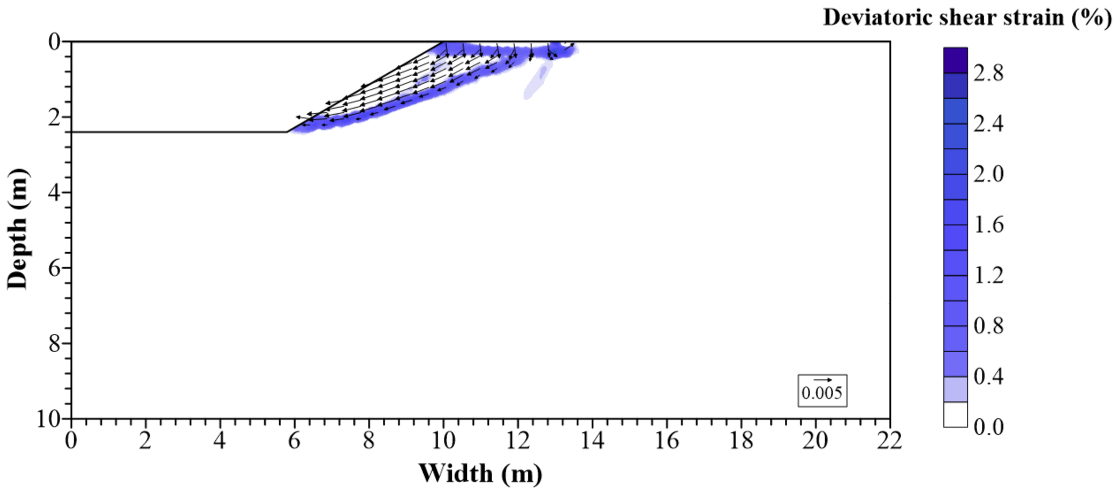

(a)

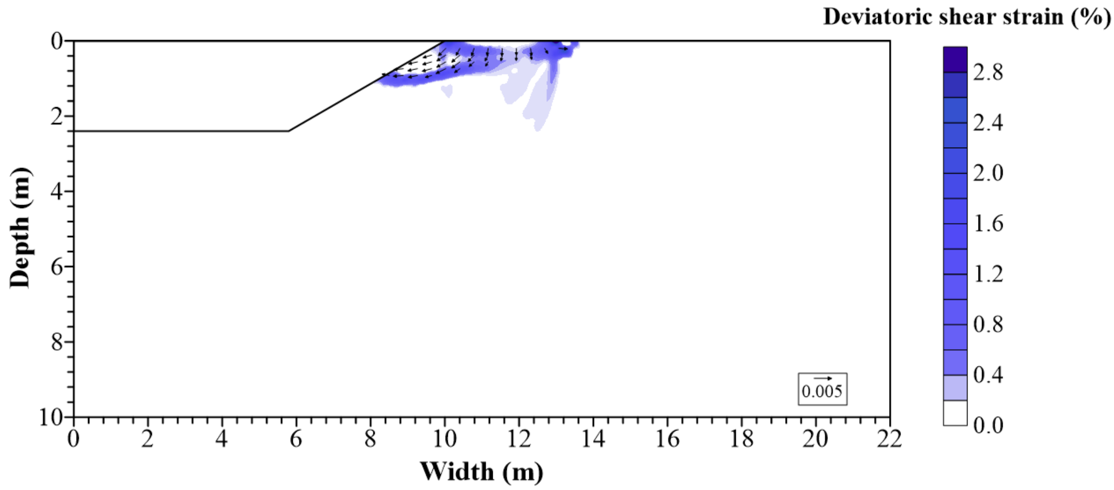

(b)

Fig. 15. Contours of the shear strain and displacement vectors for loose sand: (a) Saturated sand; (b) Gassy sand

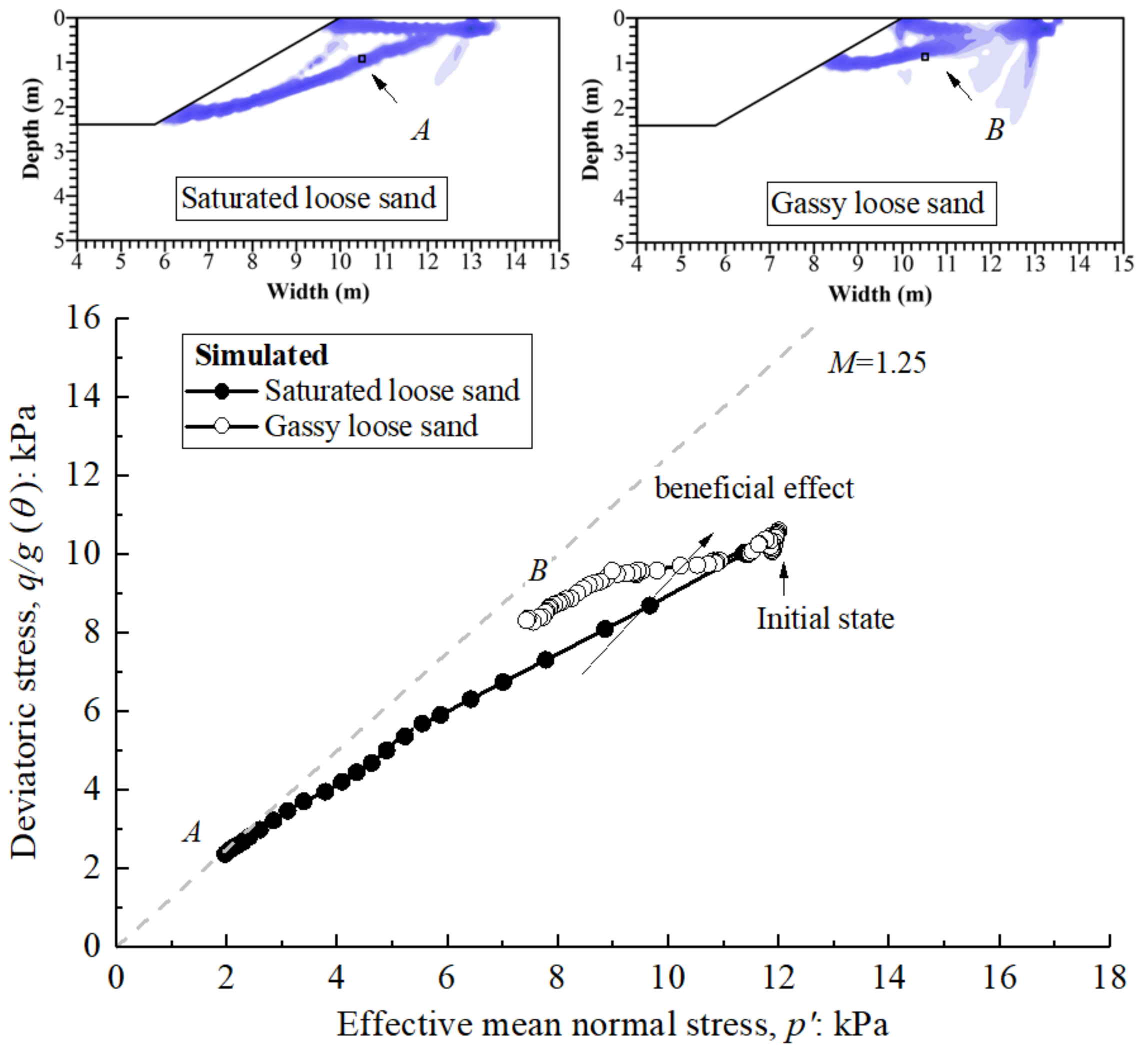

Fig. 16. Comparison of stress paths of saturated loose sand and gassy loose sand at a point in the shear zone

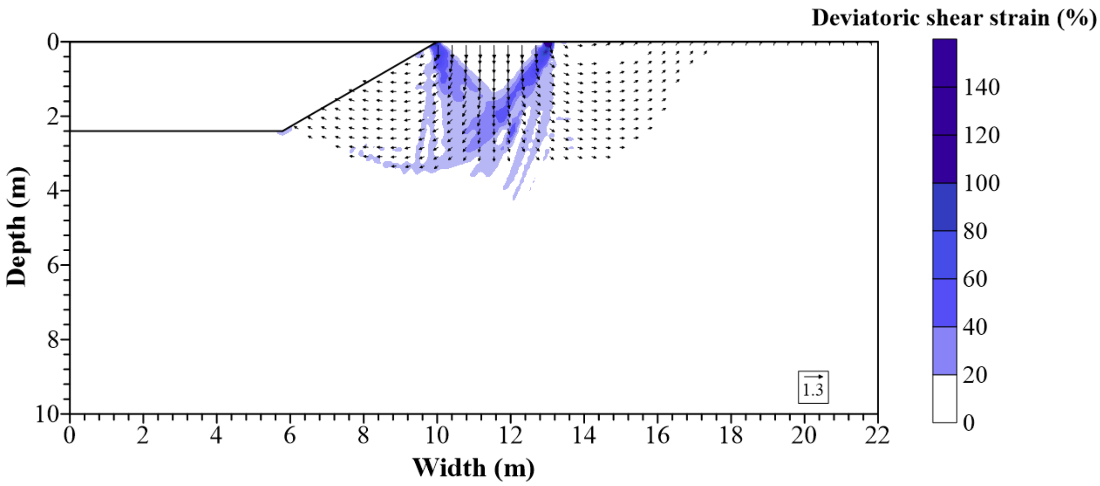

(a)

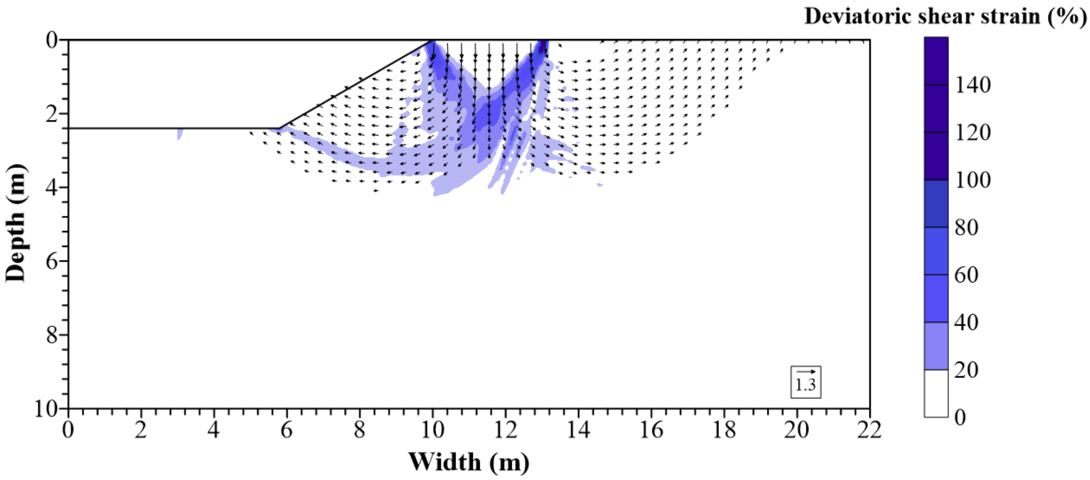

(b)

Fig. 17. Contours of the shear strain and displacement vectors for dense sand: (a) Saturated sand; (b) Gassy sand

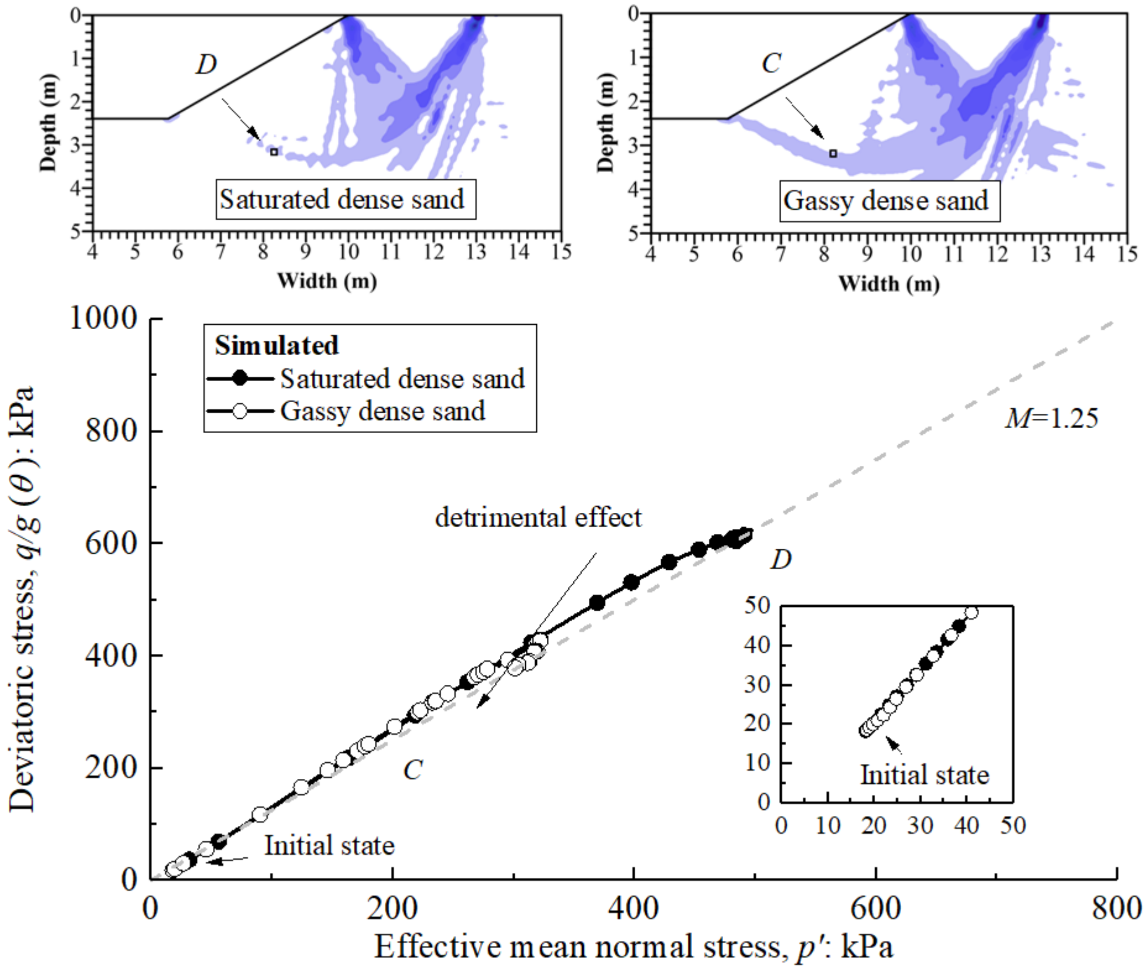

Fig. 18. Comparison of stress paths of saturated dense sand and gassy dense sand at a point in shear zone